

Chapter 8: Unconventional topology with a Rashba SOC quantum gas

As mentioned in the previous Chapter, topological order is present in a wide range of physical systems and is quantified by integer valued topological invariants such as the Chern number. In this Chapter I describe a system with Rashba-type spin-orbit coupling whose topological invariants can take half-integer values. If the concept of half-integer invariants does not sound odd, think of a donut with half a hole.

Ultracold atomic systems are an emerging platform for engineering topological lattices, from the Harper-Hofstadter model [1,2], the Haldane model [3], to the Rice-Mele model [4,5] as well as assembling spin-orbit coupled lattices without analogues in existing materials [6,7]. However, experimental realizations of topological materials have mostly focused on engineering different topological bands (with different Berry curvatures) in lattice systems, where the BZ is always a torus. Here I show that by eliminating the lattice potential and thereby changing the BZ from \mathbb{T}^2 to \mathbb{R}^2 , i.e. from a torus to a Cartesian plane, it is possible to create topological branches of the dispersion relation with half-integer Chern number.

The experiments presented here combine the experimental techniques that

were presented in Chapters ?? and ??, additionally I use the key concepts of topology described in Chapter ?. This Chapter is organized in the following way: First I give a general overview of Rashba SOC and describe theoretical proposals for engineering this type of coupling in ultracold atom systems. Then I describe our experimental implementation of Rashba SOC in the lab using a trio of Raman coupled CDD states and validate our quantum engineering using Fourier transform spectroscopy. Finally I describe a quantum state tomography procedure to measure the eigenstates of our system, from which we can directly obtain the Chern number.

To avoid confusion between dressed state xyz labels and Cartesian coordinates, in this Chapter I will use the numbers 1, 2, 3 to label the coordinates $\mathbf{e}_x, \mathbf{e}_y, \mathbf{e}_z$ and the letters x, y, z to label clock state parameters.

8.1 Rashba spin-orbit coupling

Rashba SOC [8] appears in condensed matter systems where electrons are confined in a 2D plane and experience an intrinsic out-of-plane electric field. If the electron's momentum is given by $\hbar\mathbf{k} = \hbar(k_x\mathbf{e}_x + k_y\mathbf{e}_y)$ and the electric field is $\mathbf{E} = E\mathbf{e}_z$, in the electron's moving frame there will be a momentum dependent magnetic field $\mathbf{B}_{\text{SOC}} = -\hbar\mathbf{k}/m \times \mathbf{E}/c^2 = \hbar E/mc^2(-k_y, k_x, 0)$. The interaction between the electron's spin with this field through the magnetic Zeeman interaction $-\mu \cdot \mathbf{B}_{\text{SOC}}$ gives rise to the SOC Hamiltonians

$$\hat{H}_{\text{SOC}} = \frac{2\alpha}{m}(k_y\hat{\sigma}_x - k_x\hat{\sigma}_y) \quad (8.1)$$

where $\alpha = g\mu_B E/c^2$, g is the electrons gyromagnetic ratio, μ_B is the Bohr magneton and $\hat{\sigma}_i$ are the Pauli matrices.

A can be seen in Figure 1, the Rashba dispersion relation is characterized by having a Dirac point located at $\mathbf{k} = 0$ (see Section ??) and a degenerate ground state that is described by the ring $k_x^2 + k_y^2 = \alpha^2$. If we combine Equation 8.1 with the free particle Hamiltonian the Hamiltonian can be written as $\hat{H} = (\hbar\mathbf{k} - \hat{\mathbf{A}})^2/2m$ where $\hat{\mathbf{A}} = \alpha(\hat{\sigma}_y\mathbf{e}_x - \hat{\sigma}_x\mathbf{e}_y)$ can be interpreted as a (matrix valued) non-Abelian gauge potential [9] whose elements do not commute. This term is closely related to the Berry connection discussed in Section ??. This non-Abelian gauge potential in combination with the Dirac point hints at us that a system with Rashba SOC has non-trivial topology.

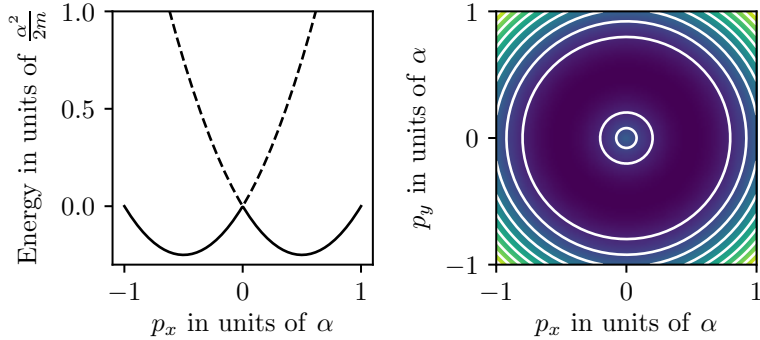


Figure 1: The Rashba dispersion relation has a Dirac point located at $\mathbf{k} = 0$ and a degenerate ground state that is described by the ring $k_x^2 + k_y^2 = \alpha^2$. [TODO: Might be nice to add the ‘hedgehog’ field as well]

SOC is a necessary ingredient for realizing \mathbb{Z}_2 topological insulators and the quantum spin-Hall effect. Furthermore, the degeneracy of the ground state single particle eigenstates could open the possibility of studying strongly correlated phases

in the presence of interactions for systems of both fermions and bosons [10–12].

Using ultracold atomic systems to engineer SOC, and in particular Rashba type SOC, has been a longstanding goal [13].

8.2 Rashba SOC for neutral atoms

Proposals for engineering Rashba type SOC in neutral atoms consist in using lasers to link internal states of an atom with its linear momentum. In order to achieve non-trivial gauge potentials it is necessary to couple $N \geq 3$ levels (see [14]). I will describe the proposal by [15] which considers a ‘ring coupling’ which is shown in Figure 2 for the case of $N = 3$. The states $|j\rangle$ represent internal atomic states and they are linked to each other with complex valued matrix elements $\frac{\Omega_j}{2} e^{i\mathbf{k}_j \cdot \mathbf{x}}$, where \mathbf{k}_j is a momentum transfer associated with the $|j\rangle \rightarrow |j+1\rangle$ transition and $\Omega_i = e^{i\phi_i} |\Omega|$ represents the coupling strength. We require that $\sum \mathbf{k}_i = 0$ so that no momentum is transferred when a closed loop $|1\rangle \rightarrow |2\rangle \cdots \rightarrow |N\rangle \rightarrow |1\rangle$ is completed. For this case the \mathbf{k}_i momenta vectors can be written as $\mathbf{k}_j = \mathbf{K}_{j+1} - \mathbf{K}_j$, and we make $\mathbf{K}_j = k_L \sin(2\pi j/N) \mathbf{e}_x + k_L \cos(2\pi j/N) \mathbf{e}_y$, corresponding to the vertices of an N sided regular polygon. We can further make a gauge transformation such that we can replace the phases ϕ_i associated to each coupling with $\bar{\phi} = \sum_i \phi_i / N$.

The Hamiltonian describing this coupling along with the kinetic term is

$$H_{j,j'} = \frac{\hbar^2 k^2}{2m} \delta_{j,j'} + \frac{\Omega}{2} (e^{i(\bar{\phi} + \mathbf{k}_j \cdot \mathbf{x})} \delta_{j,j'+1} + \text{h.c.}), \quad (8.2)$$

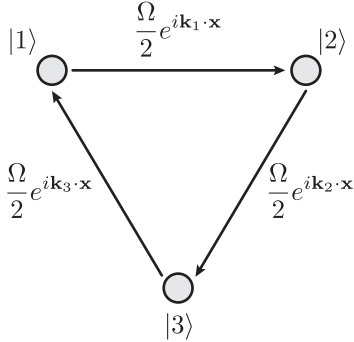


Figure 2: The Rashba ring coupling. To generate Rashba SOC in a system of cold atoms it is necessary to cyclically couple $N \geq 3$ internal states such that the transition $|j\rangle \rightarrow |j+1\rangle$ has a momentum transfer \mathbf{k}_j and $\sum_j \mathbf{k}_j = 0$ such that there is no momentum transfer for a closed loop $|1\rangle \rightarrow |2\rangle \dots |N\rangle \rightarrow |1\rangle$. The ring coupling combined with the free particle Hamiltonian give rise to a 2-level subspace that can be described to first order by the Rashba Hamiltonian

and after applying the unitary transformation $U_{j,j'} = \exp[i\mathbf{K}_i \cdot \mathbf{x}] \delta_{j,j'}$ ¹ it gets transformed to

$$H_{j,j'} = \frac{\hbar^2}{2m} |\mathbf{q} + \mathbf{K}_j|^2 \delta_{j,j'} + \frac{\Omega}{2} (e^{i\bar{\phi}} \delta_{j,j'+1} + \text{h.c.}), \quad (8.3)$$

where I have replaced the momentum \mathbf{k} by the quasimomentum \mathbf{q} . The off diagonal terms of Equation 8.3 can be related to a 1D periodic tight-binding Hamiltonian with hopping elements $\Omega/2$ where the internal states $|j\rangle$ represent lattice sites and completing one loop corresponds to gaining a ‘flux’ of $N\bar{\phi}$. To visualize how the Rashba Hamiltonian emerges from this coupling scheme, it is helpful to write the Hamiltonian in a basis that is conjugate to the index j ²

$$|l\rangle = \frac{1}{\sqrt{N}} \sum_{j=1}^N e^{i2\pi jl/N} |j\rangle \quad (8.4)$$

¹This transformation is equivalent to applying a state dependent momentum boost $\mathbf{k} \rightarrow \mathbf{k} + \mathbf{K}_j$

²Just like position and momentum are conjugate variables related by Fourier transforms, the $|j\rangle$ and $|l\rangle$ basis are related by a discrete Fourier transform.

where the index l is analogous to the crystal momentum index for a Bloch Hamiltonian. In this new basis, terms in the diagonals are displaced to the off-diagonal and likewise terms in the off diagonals are displaced to the diagonal. Under this basis the Hamiltonian starts looking very much Rashba-like

$$H_{l,l'} = \left[\frac{\hbar^2}{2m} (q^2 + k_L^2) + E_l \right] \delta_{l,l'} + \frac{\hbar^2 k_L}{m} [(iq_x + q_y) \delta_{l-1,l'} + \text{h.c.}] , \quad (8.5)$$

where $E_L = 2\hbar\Omega \cos(2\pi l/3 + \bar{\phi})$ correspond to the eigenenergies when $q = 0$. The phase $\bar{\phi}$ can be tuned such that a pair of states with consecutive l index become degenerate, indicating the presence of a Dirac point at $q = 0$. Figure 3 shows the energies E_l for $N = 3$ and $\bar{\phi} = 0$.

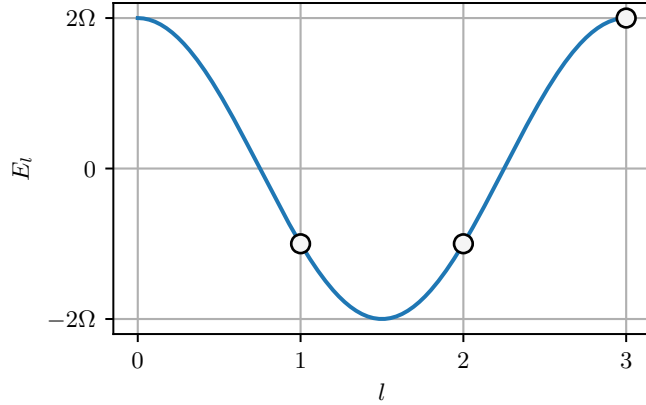


Figure 3: Eigenenergies of Equation 8.5 for $q = 0$ for $N = 3$ and $\bar{\phi} = 0$. For this particular choice of phase, the energies of the $l = 1$ and $l = 2$ states become degenerate

We can consider the degenerate states as pseudospins which are described to

zeroth order by the Rashba plus free particle Hamiltonian

$$\hat{H}^{(0)} = \frac{\hbar^2 q^2}{2m} + \frac{\hbar^2 k_L}{m} (\hat{\sigma}_x q_y - \hat{\sigma}_y q_x), \quad (8.6)$$

with spin orbit coupling strength given by $\alpha = \hbar^2 k_L / 2$. The zeroth-order Hamiltonian has continuous rotational symmetry while the proposed ring coupling only has discrete rotational symmetry. The symmetry of the Hamiltonian is recovered when higher order corrections are added to the Hamiltonian. The complete expressions for the higher order terms for $N = 3$ and $N = 4$ can be found in [15], and they are reminiscent of quadratic and cubic Dresselhaus SOC [16]. The largest leading order term for the $N = 3$ case is inversely proportional to Ω so that this ring-coupling scheme results in a more ‘Rashba-like’ Hamiltonian as one goes to higher coupling strengths. Figure 4 shows level curves of the ground state eigenenergies of Equation 8.5 for $N = 3$ and $\bar{\phi} = 0$ for increasing Ω . At low Ω the dispersion has discrete rotational symmetry and is characterized by three local minima³. As Ω is increased the local minima start merging into each other and in the large Ω limit we recover the characteristic Rashba ring-like dispersion.

8.3 Experimental implementation of Rashba SOC

We implemented the ring-coupling scheme and thereby engineered Rashba SOC by resonantly coupling the $|xyz\rangle$ states from Chapter ?? states using two-photon Raman transitions [17] as depicted in Figure 5. The engineered system

³or... an alien face?

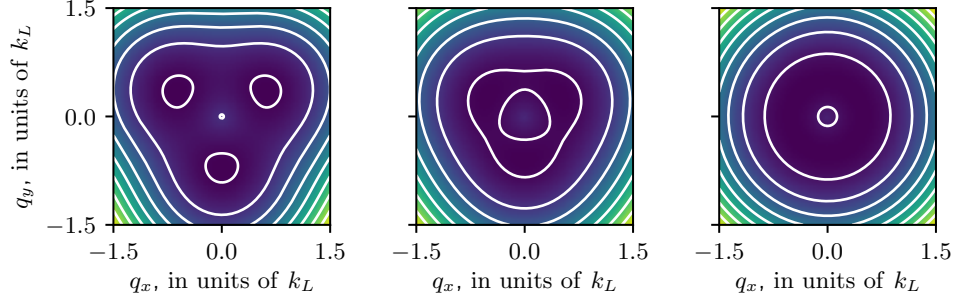


Figure 4: Ground state dispersion relation of Equation 8.5 for $N = 3$ and $\bar{\phi} = 0$ for $\Omega = 1.75 E_L$ (left), $\Omega = 3.5 E_L$ (middle) and $\Omega = 175 E_L$ (right). Higher order corrections to $\hat{H}^{(0)}$ decay as $1/\Omega^2$ and in the large Ω limit we recover the Rashba ring dispersion.

consisted of an effective spin-1/2 Rashba subspace, along with a topologically trivial high-energy branch. Our engineered Rashba system had a single Dirac cone near $\mathbf{q} = 0$, where the two lower dispersion branches become degenerate and the Berry curvature becomes singular. Each of these branches extend to infinite momentum, making the supporting manifold a plane rather than a torus. We characterized this system using both spectroscopy and quantum state tomography. This allowed us to measure the dispersion branches and directly observe the single Dirac point linking the lowest two branches as well as to reconstruct the Berry connection to derive the associated Chern numbers.

All of our experiments started with about $N \approx 1 \times 10^6$ ^{87}Rb atoms in a crossed optical dipole trap [18], with frequencies $(f_1, f_2, f_3) \approx (70, 85, 254)$ Hz, just above the transition temperature for Bose-Einstein condensation. We initially prepared the atoms in the $|F = 1, m_F = -1\rangle$ state of the $5S_{1/2}$ electronic ground state and transferred atoms to the $m_F = 0$ and $m_F = +1$ states as needed using ARP. A bias field $B_0 \mathbf{e}_3$ gave a $\omega_0/2\pi = 23.9$ MHz Larmor frequency along with a

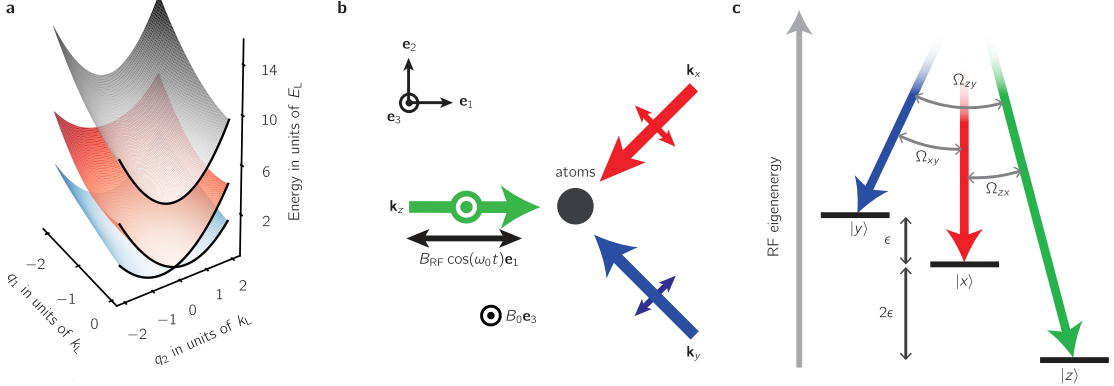


Figure 5: **a** Our engineered dispersion consisted of a two-level Rashba subspace (red and blue) with a single Dirac point linking the lowest two branches and a topologically trivial higher branch (gray). **b** We generated $|xyz\rangle$ states by combining a bias magnetic field along \mathbf{e}_3 with an RF magnetic field oscillating along \mathbf{e}_1 . These states were coupled by three cross-polarized Raman laser beams propagating along \mathbf{e}_1 , $\mathbf{e}_2 - \mathbf{e}_1$ and $-\mathbf{e}_1 - \mathbf{e}_2$. **c** Each pair of Raman lasers was in two-photon resonance with a single transition between the $|xyz\rangle$ states which we coupled strengths $(\Omega_{zx}, \Omega_{xy}, \Omega_{yz})/2\pi = (12.6(5), 8.7(8), 10(1))$ kHz.

quadratic shift of $\epsilon/2\pi = 83.24$ kHz. The RF field used to generate the $|xyz\rangle$ states and implementing CDD had strength $\Omega_{RF} = 1.41(2)\epsilon$. We adiabatically prepared the $|xyz\rangle$ states starting from the m_F states following the procedure described in Section ??.

8.3.1 Raman coupling the $|xyz\rangle$ states

We Raman-coupled atoms prepared in any of the $|xyz\rangle$ states using the three cross-polarized Raman laser beams shown in Figure 5b, tuned to the ‘magic zero’ wavelength $\lambda_L = 790$ nm. We arranged the Raman lasers into the tripod configuration shown in Figure 5c, bringing each pair into two-photon resonance with a single transition with strengths $(\Omega_{zx}, \Omega_{xy}, \Omega_{yz})/2\pi = (12.6(5), 8.7(8), 10(1))$ kHz. The ge-

ometry of our experimental implementation differs from [17] where all Raman lasers are perpendicular. We had to go away from the ideal configuration because we needed all of the Raman recoil vectors to lie on the imaging plane (spanned by \mathbf{e}_1 and \mathbf{e}_2) in order to image all the Raman induced \mathbf{k} dependent dynamics. As a result of this the dispersion relation no longer has discrete rotational symmetry, however the Dirac point is still present in our system. The only way to break the degeneracy of this system is to change the phase $\bar{\phi}$ and for our laser configuration we always have $\bar{\phi} = 0$.

The energies of the $|xyz\rangle$ states are $\omega_x = 0$ and $\omega_{z,y} = -(\epsilon \pm \sqrt{4\Omega_{\text{RF}}^2 + \epsilon^2})/2$. We set the frequencies of the Raman lasers to $\omega_x = \omega_L + \omega_0 + \omega_{xy}$, $\omega_y = \omega_L + \omega_0$ and $\omega_z = \omega_L - \omega_{zx}$, where $\omega_L = 2\pi c/\lambda_L$ and $(\omega_{zx}, \omega_{xy}, \omega_{zy})/2\pi = (166.47, 83.24, 249.71)$ kHz are the transition frequencies between pairs of dressed states and are integer multiples of ϵ for our coupling strength $\Omega = \sqrt{2}\epsilon$.

The Raman coupled states can be described by the combined kinetic and light-matter Hamiltonian

$$\hat{H}_{\text{R}}(\mathbf{k}) = \sum_{j \in \{xyz\}} \left(\frac{\hbar^2 k^2}{2m} + \hbar\omega_i \right) |j\rangle \langle j| + \sum_{j' \neq j} \hbar\Omega_{j,j'} e^{i(\mathbf{k}_{j,j'} \cdot \mathbf{x} - i\omega_{j,j'} t)} |j\rangle \langle j'|, \quad (8.7)$$

where $\mathbf{k}_{j,j'}$ is the recoil momentum from an $|j\rangle \rightarrow |j'\rangle$ transition and Ω_{ij} is the Raman coupling strength between a pair of RF dressed states. The Hamiltonian above only includes the matrix elements associated to resonant couplings. We apply the unitary transformation $\hat{U}_{j,j'} = \exp(-i\mathbf{k}_j \cdot \mathbf{x} - \omega_j t) \delta_{j,j'} |j\rangle \langle j'|$ so that the Hamiltonian takes

the familiar form of the ring coupling scheme

$$\hat{H}_R = \sum_{j \in \{xyz\}} \left(\frac{\hbar^2(\mathbf{q} - \mathbf{k}_j)^2}{2m} + \hbar\delta_j \right) |j\rangle \langle j| + \sum_{j \neq j'} \hbar\Omega_{jj'} |j\rangle \langle j'|, \quad (8.8)$$

where \mathbf{k}_j are the Raman wave vectors and δ_j is the detuning from Raman resonance.

This coupling scheme simultaneously overcomes three limitations of earlier experiments [19, 20] that performed the ring coupling using states in both $5S_{1/2}$ hyperfine manifolds of ^{40}K : (1) working in the same hyperfine manifold eliminates spin-relaxation collisions [21]; (2) unlike m_F states, the $|xyz\rangle$ states can be tripod-coupled with lasers far detuned relative to the excited state hyperfine splitting greatly reducing spontaneous emission [22]; and (3) CDD renders the $|xyz\rangle$ states nearly immune to magnetic field noise.

8.3.1.1 Floquet and off resonant coupling effects

We operated in a regime where the transition energies between the $|xyz\rangle$ states were integer multiples of ω_{xy} : $\omega_{zx} = 2\omega_{xy}$ and $\omega_{zy} = 3\omega_{xy}$, and therefore we can use Floquet theory for a complete description of our system [23]. We observed that the effective Raman coupling strengths for the driven three level system differed from our calibrations which were performed looking at Rabi oscillations from individual pairs of lasers because of the presence of nearby quasi-energy manifolds and off resonant coupling terms. This effect could be mitigated for larger values of ω_{xy} as the spacing between quasi-energy manifolds is increased and the off resonant coupling terms less relevant. Appendix ?? has a full derivation of the Raman Hamiltonian starting from

the $|m_F\rangle$ basis in the lab frame including the full time dependence and off resonant coupling terms.

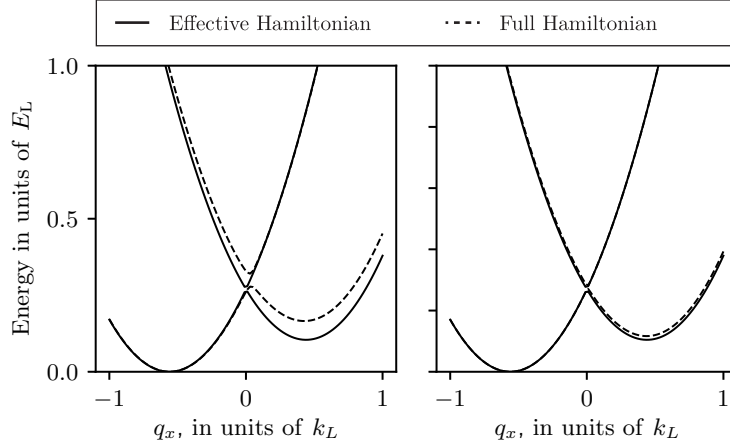


Figure 6: Solid lines: Dispersion relation from RWA Hamiltonian (Equation 8.8) as a function of q_x for $\Omega_{i,j} = 1.5 E_L$ and $\delta_i = 0$. Dashed lines: Dispersion relation computed for the full Floquet Hamiltonian. We considered $\omega_{zx} = 2\omega_{xy}$ and $\omega_{zy} = 3\omega_{xy}$ in both cases so the separation between Floquet manifolds is ω_{xy} . In the left panel $\omega_{xy} = 83.24$ kHz as in our experiments and in the right panel $\omega_{xy} = 416.2$ kHz. As the spacing between Floquet manifolds becomes we get a better agreement between the spectra of the RWA and Floquet Hamiltonians.

8.3.1.2 Lifetime

The limited lifetime due to spontaneous emission has always been a concern for Raman coupled systems. This was in part one of the reasons why we pursued the topology direction rather than trying to measure a fragile many-body phase. The measured spontaneous emission limited lifetime of our system was 320(17) ms, measured with the Raman lasers applied to the m_f states. However, it was reduced to 40(2) ms when we Raman coupled the $|xyz\rangle$ states, which we attribute to technical noise in the relative phase between the RF dressing field and the Raman laser

fields, which has caused considerable consternation in ongoing experiments. All the experiments reported here were short compared to this timescale so this decreased lifetime was not an issue but it is a limitation that needs to be addressed in future experiments. Figure 7 shows measurements of the lifetimes of Raman dressed atoms in both $|m_f\rangle$ and $|xyz\rangle$ states. We obtained the lifetime by fitting decaying exponentials to the integrated OD obtained from absorption images of thermal atoms where the Raman was turned on in 1 ms and held on for up to $50 \mu\text{s}$ ⁴.

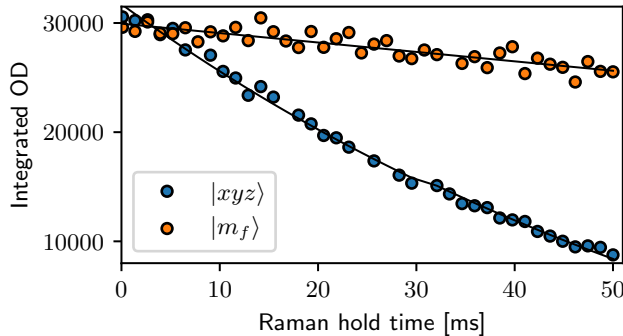


Figure 7: Lifetime of Raman dressed states. We Raman dressed atoms in the $|m_f\rangle$ and $|xyz\rangle$ states. The orange markers correspond to atoms initially prepared in $|m_f = -1\rangle$ (no high power RF involved) and the blue markers correspond to atoms $|xyz\rangle$ (three averaged traces). The lifetime of doubly dressed states is significantly reduced as compared to the lifetime of the Raman dressed $|m_f\rangle$ states, indicating that resonant scattering of photons is not our only loss mechanism.

8.3.2 Measuring quasimomentum distributions

Each pair of Raman lasers coupled states $|i, \mathbf{k}\rangle \rightarrow |j, \mathbf{k} + \mathbf{k}_{i,j}\rangle$ where $|i\rangle$ and $|j\rangle$ denote the initial and final $|xyz\rangle$ states, \mathbf{k} is the initial momentum and $\mathbf{k}_{i,j} = \mathbf{k}_i - \mathbf{k}_j$ is the two-photon Raman recoil momentum. Dressed states with quasimomentum \mathbf{q}

⁴How long we could hold on the Raman was limited by the RF antenna heating up.

are comprised of three bare states $|j, \mathbf{k}\rangle$ with momentum $\mathbf{k} = \mathbf{q} - \mathbf{k}_j$. The eigenstates of our Rashba SOC Hamiltonian take the form

$$|\Psi_n(\mathbf{q})\rangle = \sum_{j \in xyz} \sqrt{a_{n,j}(\mathbf{q})} e^{i\phi_{n,j}(\mathbf{q})} |j, \mathbf{k} = \mathbf{q} - \mathbf{k}_j\rangle, \quad (8.9)$$

where the quasimomentum \mathbf{q} is a good quantum number and the amplitudes are parametrized by $a_{n,j}(\mathbf{q})$ and $\phi_{n,j}(\mathbf{q})$. We leveraged the wide momentum distribution of a non-condensed ensemble ($T \approx 180$ nK and $T/T_c \approx 1.1$) to sample a wide range of momentum states simultaneously. By starting separately in each of the $|xyz\rangle$ states we sampled the range of quasimomentum states shown in Figure 8b, where the momentum distributions of an initial state $|j, \mathbf{k}\rangle$ is shifted from $\mathbf{q} = 0$ by the corresponding Raman wave vector \mathbf{k}_j .

Our measurement protocol consisted of abruptly removing the confining potential and the Raman lasers, initiating a 21 ms TOF. During this TOF we adiabatically transformed each of the $|xyz\rangle$ states back to a corresponding $|m_F\rangle$ state following the procedure described in Section ?? and spatially separated them using a Stern-Gerlach gradient. Finally we used resonant absorption imaging to measure the resulting spin-momentum distributions.

The FWHM of the cloud after TOF is about $700 \mu\text{m}$ which is much larger than the size of the in-situ cloud $\sim 50 \mu\text{m}$ and therefore the spatial density distribution of the TOF images represents momentum distribution of the atoms. For the $7.4 \mu\text{m}$ pixel size of our camera and the 3.283 magnification of our imaging system, the momentum resolution of our images was 0.018 k_L and the momentum distribution

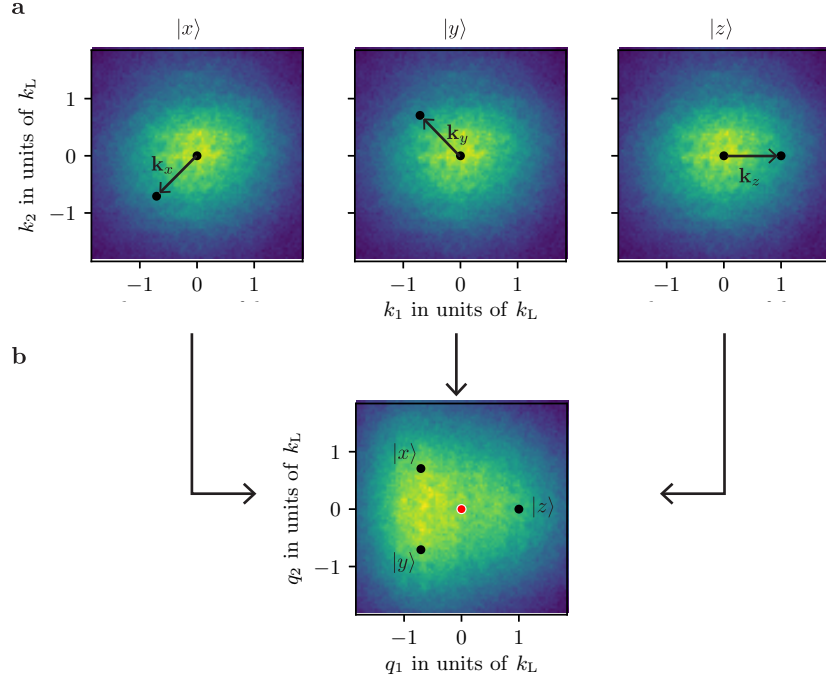


Figure 8: Mapping momentum into quasimomentum: **a** We used non-condensed atoms with a broad momentum distribution ($T \approx 180$ nK and $T/T_c \approx 1.1$). **b** Atoms in $|j, \mathbf{k}\rangle$ are mapped to Raman dressed states with quasimomentum $\mathbf{q} = \mathbf{k} + \mathbf{k}_j$. The black dots in the bottom panel represent the location of $\mathbf{k} = 0$ for each of the $|xyz\rangle$ states and the red dot corresponds to $\mathbf{q} = 0$. We performed our experiments starting separately in each of the $|xyz\rangle$ states, which allowed us to sample a larger range of quasimomentum states.

of a single state measured after TOF had a FWHM of $\sim 2.2 k_L$.

8.3.2.1 Correcting shears from Stern-Gerlach gradient

The magnetic field gradient used to separate the different m_f states in TOF additionally creates a trap for atoms in the direction perpendicular to the Stern-Gerlach separation, causing a compression (expansion) of the $m_f = -1$ (+1) states (see Section ??). The faster moving atoms are subject to a stronger potential and therefore the projections of a given momentum state \mathbf{k} along the Stern-Gerlach axis

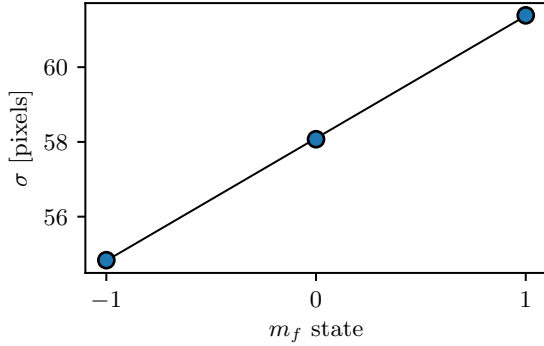


Figure 9: We measured the standard deviation of the momentum distribution along the axis perpendicular to the SG for 10 shots on each m_f state. From the slope of the linear fit we obtain a shearing parameter $\alpha \approx \pm 0.067$ for $m_f = \pm 1$.

and perpendicular to it were transformed as $k_{\parallel} \rightarrow k_{\parallel}$ and $k_{\perp} \rightarrow (1 + \alpha)k_{\perp}$, where $\alpha = 0$ for $m_f = 0$ and $\text{sign}(\alpha) = \pm 1$ for $m_f = \pm 1$.

Since we were interested in mapping the momentum distribution of atoms it was important for us to quantify and correct the effect of these shears in the TOF images. We used two different methods: First we prepared thermal atoms in all three of the m_f states and fit 2D Gaussians rotated by the angle of the SG displacement; 63.8 degrees for our images. Figure 9 shows the standard deviation extracted from the Gaussian fits along the axis perpendicular to the SG deviation as a function of m_f state. We performed a linear fit of σ and found that the $m_f = \pm$ states are expanded/contracted by about $\pm 6.7\%$ size of the compared to the $m_f = 0$ cloud ($\alpha = \pm 0.067$).

Alternatively we performed the Ramsey interferometer described in Section 8.5 but coupling only 2 states, either $|z\rangle \leftrightarrow |x\rangle$ or $|x\rangle \leftrightarrow |y\rangle$ (mapped to $| -1 \rangle \leftrightarrow | 0 \rangle$ and $| 0 \rangle \leftrightarrow | +1 \rangle$ after TOF). We looked at the oscillation frequencies of the density

for each pixel of the CCD camera (each sheared momentum state) and fit them to Equation 8.17 for fixed value of the recoil momentum $\mathbf{k}_{i,j}$ and with a free shear parameter that modifies \mathbf{q} . Using this method we extracted a shearing of the order of 7%, in good agreement with the Gaussian fitting method.

The transformed momentum coordinates were described by a function

$$g(\mathbf{k}) = (k_{\parallel}, (1 + \alpha)k_{\perp}) \quad (8.10)$$

and our observed data $(y_i^{(\text{shear})}, \mathbf{k}^{(\text{shear})})$ was the density in the sheared coordinate system at the i th pixel of the CCD sensor. The density in the unsheared coordinate was estimated using

$$y_j = \frac{\sum_i \exp[-(g(\mathbf{k}_j) - \mathbf{k}_i^{(\text{shear})})^2/2\sigma^2] y_i^{(\text{shear})}}{\sum_i \exp[-(g(\mathbf{k}_j) - \mathbf{k}_i^{(\text{shear})})^2/2\sigma^2]}, \quad (8.11)$$

where σ is the spacing between two consecutive pixels ($\sim 0.018 k_L$). Prior to any data analysis we applied this transformation to all of our images, where we used different values of α that define $g(\mathbf{k})$ for each of the m_f states.

8.4 Fourier spectroscopy of the Rashba dispersion

We directly measured the 2D dispersion relation using Fourier transform spectroscopy [24]. We considered the evolution of an initial state $|i, \mathbf{k}\rangle$ suddenly subjected to the Raman coupling lasers. This atomic Rabi-type interferometer is analogous to the three-port beam-splitter depicted in Figure 10a. During a pulse time t_p

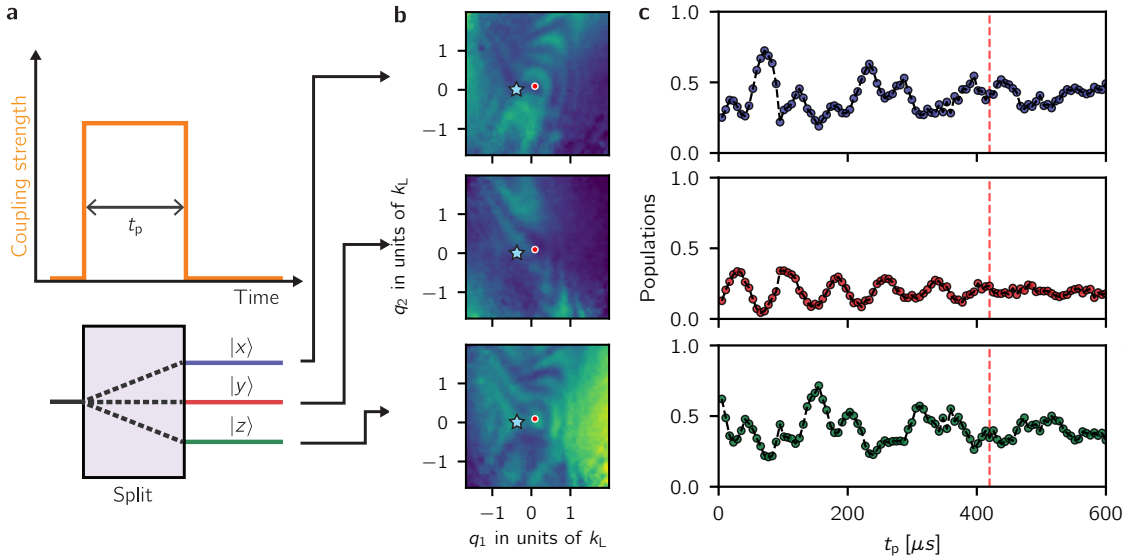


Figure 10: **a** Fourier spectroscopy protocol. We applied the Raman lasers for a variable time t_p : a Rabi-type atomic interferometer analogous to a three-port beam splitter. **b** Probabilities as a function of quasimomentum for a fixed Raman pulse time $t_p = 420 \mu\text{s}$ **c** Dynamics of the final populations of the $|xyz\rangle$ states with quasi-momentum $(q_1, q_2) = (-0.55, -0.18) k_L$ (blue star in panels **b**) after initializing the system in the $|z\rangle$ state.

we followed the dynamics of the populations in the $|xyz\rangle$ states which evolved with oscillatory components proportional to $\sum_{j \neq n} a_{n,j}(\mathbf{q}) \cos([E_n(\mathbf{q}) - E_j(\mathbf{q})]t_p / \hbar)$, with frequencies determined by the eigenenergy differences $E_n - E_j$. Figure 10b shows the momentum dependent populations for a fixed pulse time t_p and Figure 10c shows representative final populations as a function of t_p for a fixed quasimomentum state. We Fourier transformed the populations with respect to t_p and for a given quasimomentum state for a total of 9 state, all of them with the same \mathbf{q} accounting for each of the three initial $|xyz\rangle$ states that was then split into 3 states. Figure 11 shows the PSD computed for each of the 9 states for planes of constant q_1 . The amplitude of the oscillatory components depends on the overlap integral between the initial

state and the Raman dressed states (see Equation ??) so sampling all these states gave us access to a wider range of measurable frequencies. The spectral maps in Figure 12b were produced by averaging the PSDs from the 9 different states using \bar{n} , the mean population in t_p , as a weight:

$$\text{PSD}^{(\text{mean})}(\mathbf{q}) = \frac{\sum_{i,j} \text{PSD}_{i,j}(\mathbf{q}) \bar{n}_{i,j}(\mathbf{q})}{\sum_{i,j} \bar{n}_i j(\mathbf{q})}, \quad (8.12)$$

where the indices i, j represent the different states of the grid shown in Figure 11. The extrema in the spectral maps are the energy differences $E_n - E_j$ in the engineered dispersion (Figure 10a). Figure 12 was obtained by combining all the spectral maps, and together they show the presence of a single Dirac point in the Rashba subspace, evidenced by the gap closing near $\mathbf{q} = 0$ and the photon-like lower branch. The dashed curves correspond to the energy differences computed for our system using the dispersions shown in Figure 12a, and are in clear agreement with our experiment. This measurement directly confirms the expected set of energies, including the existence of a two-state subspace approximately described by the Rashba Hamiltonian.

8.5 Quantum state tomography with Ramsey interferometer

The Fourier spectroscopy measurement confirmed our quantum engineering of the Rashba Hamiltonian. However, the energies shed no light on the topology of the different branches of the dispersion, which instead requires knowledge of the eigenstates. The Berry curvature present in the definition of the Chern number (Equa-

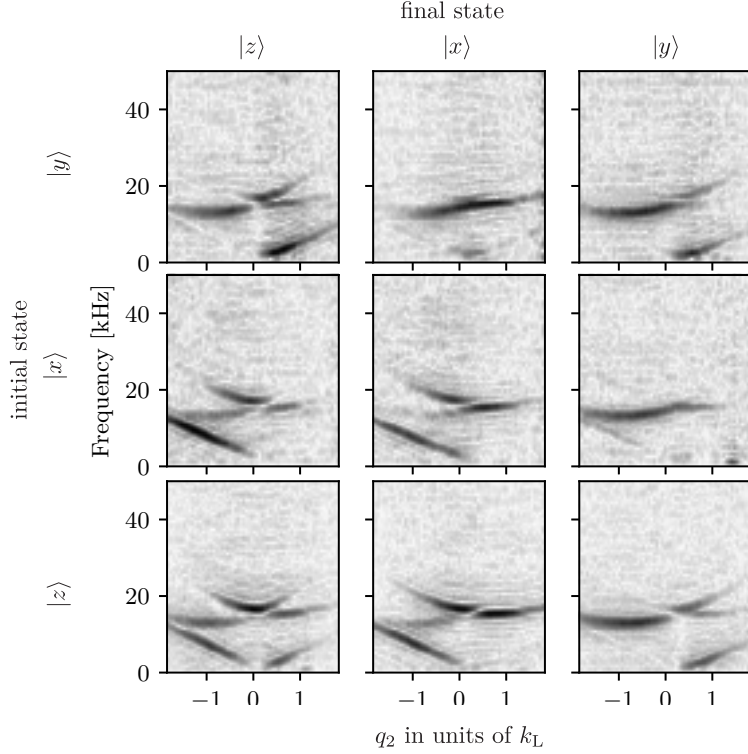


Figure 11: PSD of all the analyzed states as a function of q_2 for fixed $q_1 = 0.18 k_L$. The different overlaps between the initial state, the Raman dressed states and the measured final state result in peaks with different amplitudes.

tion ??) can be derived from the Berry's connection $\mathbf{A}_n(\mathbf{q}) = i \langle \Psi_n(\mathbf{q}) | \nabla_q | \Psi_n(\mathbf{q}) \rangle$, which as discussed in Chapter ?? behaves much like a vector potential in classical electromagnetism. The Berry curvature $\Omega_n(\mathbf{q}) = \nabla_q \times \mathbf{A}(\mathbf{q})$ is the associated magnetic field and the flux through any surface is the line integral of $\mathbf{A}(\mathbf{q})$ along its boundary, after neglecting the contributions of Dirac strings which I will discuss later. Using the expression for the Raman dressed eigenstates from Equation 8.9 we obtain

$$\mathbf{A}_n(\mathbf{q}) = - \sum_{j \in \{x,y,z\}} a_{n,j}(\mathbf{q}) \nabla_q \phi_{n,j}(\mathbf{q}), \quad (8.13)$$

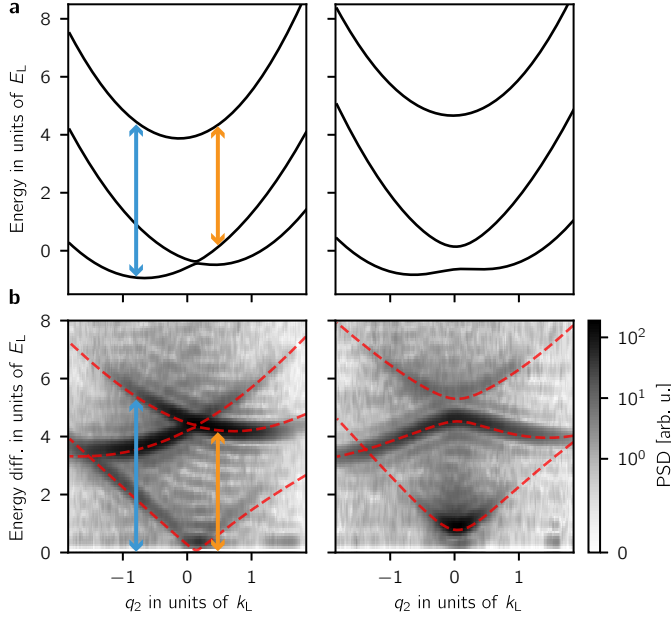


Figure 12: **a** Predicted dispersion relation as a function of q_2 for fixed $q_1 = -0.09 k_L$ (left) and $0.65 k_L$ (right), computed for the experiment parameters. The energy differences between the branches enclosing the vertical arrows appear as peaks in the spectral maps below. **b** Power spectral density (PSD) for the same parameters as above which we obtained by Fourier transforming the populations in the $|xyz\rangle$ states with respect to t_p . The dashed lines correspond to the energy differences computed using the dispersion curves on the top panel.

which depends on both the phase and amplitude of the wave function. We obtained $a_{n,j}(\mathbf{q})$ and $\phi_{n,j}(\mathbf{q})$ using a three-arm time-domain Ramsey interferometer (see Section ??), implementing a variant of quantum state tomography [25, 26]. The use of a multi-path interferometer allowed us to transduce information about phases into state populations, which we readily obtained from absorption images.

Figure 13 shows our experimental protocol which I will describe in more detail in the following section. We adiabatically mapped an initial $|j, \mathbf{k}\rangle$ state into a corresponding eigenstate $|n, \mathbf{q} = \mathbf{k} + \mathbf{k}_j\rangle$, either in the topologically trivial highest dispersion branch ($n = 3$) or in the topological ground branch ($n = 1$) by dy-

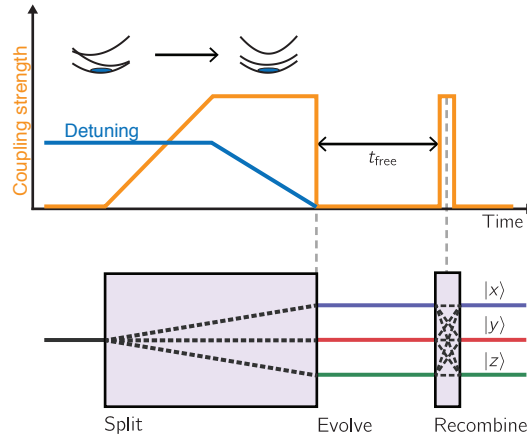


Figure 13: Experimental protocol for three-arm Ramsey interferometer (not to scale). (Top) We started with atoms in state $|z, y, \mathbf{q}_i = \mathbf{k} + \mathbf{k}_j\rangle$ and with detuning $\delta_y = \pm 5 E_L$ and $\delta_z = \pm 5 E_L$. We ramped the Raman lasers on in $750 \mu\text{s}$ and then ramped the detuning to nominally zero. We let the system evolve in the dark for times between $5 \mu\text{s}$ and $400 \mu\text{s}$, followed by a $25 \mu\text{s}$ Raman pulse. (Bottom) The implemented experimental protocol was equivalent to a three-arm interferometer that split an initial state into three final states with amplitudes related to the initial wave function phases.

namically tailoring both the Raman coupling strength and detuning. We suddenly turned off the Raman coupling, thereby allowing the three bare state components of the Rashba eigenstates to undergo free evolution for a time t_{free} , constituting the three arms of our time-domain interferometer. Finally we applied a three-port beam splitter using a brief Raman ‘recombination’ pulse to interfere the three arms.

8.5.1 Wave function evolution in Ramsey interferometer

Rashba dressed state preparation: We started with $|xyz\rangle$ states at different RF coupling strength $\Omega_0 = \Omega_{\text{RF}}/\pi 2 \pm 20 \text{ kHz}$, such that the energies of the $|z\rangle$ and $|y\rangle$ states were shifted by about $\pm 18.8 \text{ kHz}$. We used the same Raman frequencies as described earlier and therefore the change in the $|xyz\rangle$ state eigenenergies

corresponded to non-zero δ_z and δ_y in Equation 8.8. We chose the detuning such that the initial state had a large overlap with either the $n = 1$ or the $n = 3$ eigenstates of Equation 8.8. We then ramped on the Raman coupling in $750\ \mu\text{s}$, adiabatically mapping the $|z\rangle$ and $|y\rangle$ states into the $n = 1$ or $n = 3$ eigenstates. Because our only experimental knob for dynamically changing the detuning was Ω_{RF} we could not control δ_x so when we initialized the system in $|x\rangle$ the the final dressed state always corresponded to the $n = 2$ branch. After turning on the Raman we ramped Ω_{RF} to its final value in $1\ \text{ms}$, effectively ramping δ_z and δ_y close to zero. This detuning ramp had the additional effect of moving the location Dirac point through the atoms when loaded in the $n = 1$ branch, thereby creating a trajectory where the state preparation was not adiabatic. This trajectory depended on the sign of the detuning ramp so we combined data from different initial states in order to exclude the Dirac point trajectories. Near the final location of the Dirac point the state preparation can not be adiabatic regardless of the initial state or detuning used for the ground state preparation. Figure 14a shows an example an absorption image of atoms initially prepared in the $|y\rangle$ state and with δ_y such atoms are loaded in the $n = 1$ branch. The Dirac point is initially located near the lower left edge of the cloud and when δ_i was ramped the location of the Dirac point was dragged across the whole cloud leaving lines where non-adiabatic transitions occurred as can be seen in Figure 14b. The location of the Dirac point as a function of δ_i can also be directly computed by numerically diagonalizing the SOC Hamiltonian from Equation 8.8. At the end of this stage, excluding the points of non-adiabatic transitions, the state of the system was described by the eigenstates in Equation 8.9.

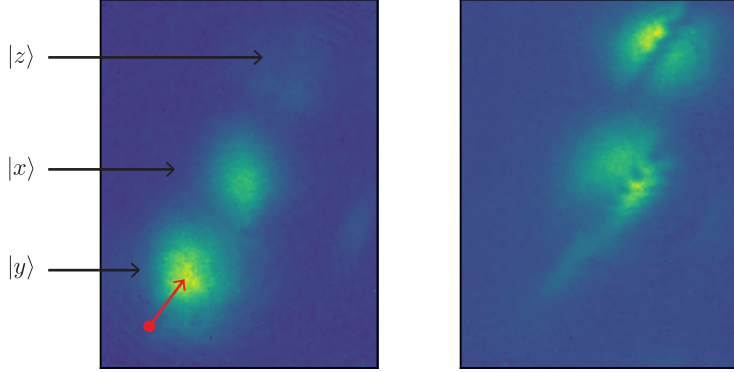


Figure 14: **a** We prepared atoms in the $|y\rangle$ state such that they are adiabatically mapped to the ground dispersion branch. **b** We ramped δ_i and dragged the Dirac point through the atoms.

Free evolution: We suddenly turned off the Raman coupling, thereby projecting the Raman dressed states back into the $|xyz\rangle$ basis. Each of the $|xyz\rangle$ state represents a different branch of the interferometer and they acquire phases that are proportional to t_{free}

$$|\Psi_n(\mathbf{q})\rangle \rightarrow \sum_{j \in xyz} \sqrt{a_{n,j}(\mathbf{q})} e^{i\phi_{n,j}(\mathbf{q})} e^{-iE_j(\mathbf{q})t_{\text{free}}/\hbar} |j, \mathbf{k} = \mathbf{q} - \mathbf{k}_j\rangle, \quad (8.14)$$

where $E_j(\mathbf{q}) = \hbar^2 \mathbf{q}^2 / 2m$ is the free particle energy. The Rashba wavefunction phases $\phi_{n,j}(\mathbf{q})$ that we were interested in measuring were imprinted during the loading procedure. The dynamical phases $E_j(\mathbf{q})t_{\text{free}}/\hbar$ acquired in the different interferometer arms does not contribute to our knowledge of the Rashba eigenstates as they describe the evolution of the system in the absence of Raman dressing.

Recombination pulse: We applied a 25 us Raman pulse that acted as a second beam splitter in our interferometer sequence. The wave function after the

pulse is

$$|\Psi(\mathbf{q})\rangle = \sum_{j,j' \in xyz} \sqrt{a_{n,j}(\mathbf{q})} e^{i(\phi_{n,j}(\mathbf{q}) - E_j(\mathbf{q})t_{\text{free}}/\hbar)} U_{j,j'}(\mathbf{q}) |j, \mathbf{k} = \mathbf{q} - \mathbf{k}_j\rangle, \quad (8.15)$$

where $U_{j,j'}(\mathbf{q}) = |U_{j,j'}(\mathbf{q})| \exp(i\phi_{j,j'}^{\text{(pulse)}}(\mathbf{q}))$ is the matrix element of the unitary transformation $\exp(i\hat{H}_{\text{R}}(\mathbf{q})t_{\text{pulse}})$ associated to the Raman pulse. At the end of this procedure, the population in a final state $|l, \mathbf{q}\rangle$ is

$$P_l(\mathbf{q}, t) = \sum_{i \neq j} |U_{l,i}| |U_{j,l}| \sqrt{a_{n,i} a_{n,j}} \cos(\omega_{i,j}(\mathbf{q})t + \phi_{n,i}(\mathbf{q}) - \phi_{n,j}(\mathbf{q}) + \phi_{l,i,j}^{\text{(pulse)}}(\mathbf{q})), \quad (8.16)$$

which directly reads out the phase differences, independent of the output port l . Here $\phi_{l,i,j}^{\text{(pulse)}}(\mathbf{q})$ is a smoothly varying phase imprinted by the recombination pulse and is independent of \mathbf{q} in the limit of short, strong pulses and does not affect the topological index of the system. The angular frequencies

$$\omega_{i,j}(\mathbf{q}) = \hbar \mathbf{q} \cdot \mathbf{k}_{i,j} / m + \delta_{i,j} \quad (8.17)$$

result from the known free particle kinetic energy, the recoil momenta and detuning $\delta_{i,j}$ from the tripod resonance condition. Figure 13b shows the momentum-dependent populations in each output port at fixed $t_{\text{free}} = 160 \mu\text{s}$ and Figure 13c shows the populations as a function of t_{free} for a representative quasimomentum state $(q_1, q_2) = (0.55, -0.92) k_{\text{L}}$.

We obtained the relative phases $\Delta\phi_{n,i,j,l}(\mathbf{q}) = \phi_{n,i}(\mathbf{q}) - \phi_{n,j}(\mathbf{q}) + \phi_{l,i,j}^{\text{(pulse)}}(\mathbf{q})$ from Equation 8.16 by fitting the measured populations to the sum of three cosines

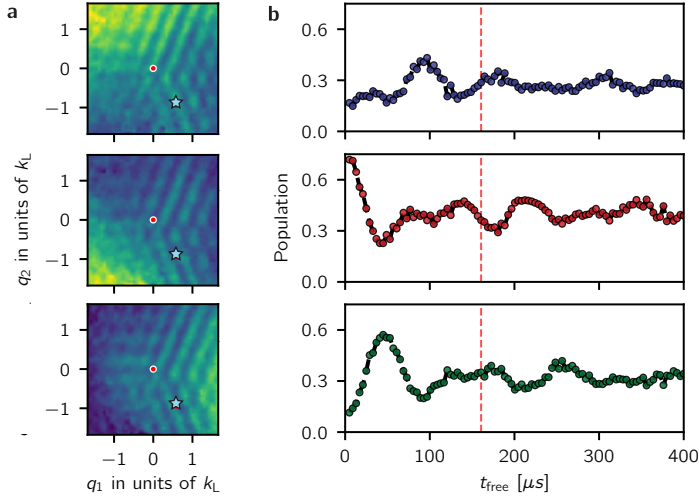


Figure 15: **a** Probabilities as a function of quasimomentum for the three output ports of the interferometer at $t_{\text{free}} = 160 \mu\text{s}$ **b** Probabilities as a function of free evolution time t_{free} for an input state with quasimomentum $(q_1, q_2) = (0.55, -0.92) k_L$ indicated by the blue star on **a** and in the topological ground branch ($n = 1$)

with the known free particle frequencies but unknown amplitudes and phases.

8.5.2 Combining phases from different measurements

We combined the phases $\Delta\phi_{n,i,j,l}(\mathbf{q})$ obtained from fits to six different states (two initial states split into 3 states). Similar to the Fourier spectroscopy measurements, we performed a weighted average of the fitted relative phases

$$\Delta\phi_{n,i,j}(\mathbf{q}) = \frac{\sum_l \Delta\phi_{n,i,j,l}(\mathbf{q}) w_{i,j,l}(\mathbf{q})}{\sum_l w_{i,j,l}(\mathbf{q})}, \quad (8.18)$$

where the weights are determined using fit uncertainties and when loading atoms in the topological branch we additionally accounted for the trajectory of the Dirac point during the loading procedure. Figure 16 shows an example of two different weight arrays used to combine the phase difference associated to the $z \rightarrow x$ transition

$i, j = z, x$ for the topological branch $n = 1$ ($\Delta_{1,z,x}$):

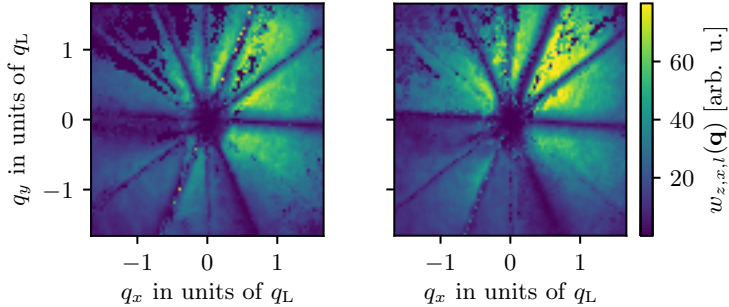


Figure 16: Two sample weight arrays $w_{i,j,l}(\mathbf{q})$ for $i, j = z, x$ and atoms prepared in the topological disperion branch. We obtained the weights using the uncertainties from the fits and the trajectory of the Dirac point during the state preparation. We combined the weights and the phase differences $\Delta\phi_{n,i,j,l}$ obtained from the time dependent fits using Equation 8.18 to obtain the phase maps displayed in Figure 17a

The ‘spokes’ in the weight arrays correspond to high uncertainty regions. This uncertainty comes of our inability to resolve the phases of low frequencies $\omega_{ij}(\mathbf{q})$ as well as when two different frequencies $\omega_{ij}(\mathbf{q})$ and $\omega_{i'j'}(\mathbf{q})$ are close to each other which is limited by the largest value of t_{free} in the experiment. I fit and combined a total of 120,000 different time traces (60,000 for each dispersion branch) to produce phase maps like those shown in Figure 17a.

8.5.3 Measuring the topological index

Figure 17a shows typical phase-maps for both the non-topological and topological branches. In the non-topological phase-maps the momentum dependence of the recombination pulse $\phi_{l,i,j}^p(\mathbf{q})$ causes a smooth variation of the phases along the Raman recoil axes that does not affect the evaluation topological index of our system. We recovered the phases $\phi_{n,j}$ of the full spinor wave function from the relative

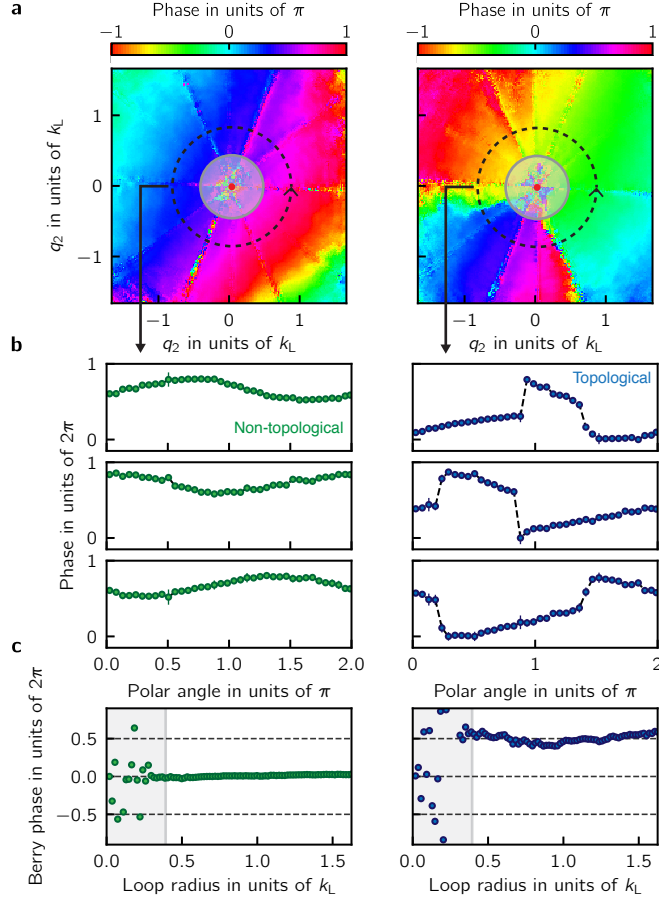


Figure 17: Topological invariants from quantum state tomography, for the non-topological branch ($n = 3$, left) and the topological branch ($n = 1$, right). **a** Phase differences as a function of quasimomentum from the the $z \rightarrow x$ transition **b** Phase differences as a function of polar angle for a loop radius $0.77 k_L$ from the $z \rightarrow x$ (top), $x \rightarrow y$ (middle) and $y \rightarrow z$ (bottom) transitions. The phases associated to the topological branch are characterized by two π valued discontinuities. Each row of phases was shifted by a constant value so that the three rows of phases share the same vertical axis. All phases shown here were binned and averaged using the fit uncertainties as weights. **c** Inferred Chern number as a function of loop radius. For loops with $q > 0.4 k_L$ we obtained an integrated Berry phase and asymptotic Chern number of $\Phi_B/2\pi = 0.01(1)$ for the non-topological branch and $\Phi_B/2\pi = 0.5(5)$ for the topological branch.

phases $\Delta\phi_{n,i,j}(\mathbf{q})$ by choosing a particular gauge such that $\phi_{n,3} = 0$. We then used the values of $a_{n,i}$ obtained from measuring the populations in the $|xyz\rangle$ states at $t_{\text{free}} = 0$ in combination with the phases of the wave function to compute the Berry

connection [27]. Figure 17b shows the three phase differences as a function of polar angle for a loop of radius $q \approx 0.77 k_L$. In addition to the smooth variations induced by the recombination which are present in both columns, the phases of the topological branch have two π valued jumps that lead to non-zero Berry phases when the Berry connection is integrated along a closed loop in momentum space. Figure 17c shows the integrated Berry phase as a function of loop radius. As mentioned earlier the largest value of t_{free} limits how well we can resolve the phases of small frequencies and this is reflected in the large variation in the Berry phase depicted in the shaded region of Figure 17c near $q = 0$. For loops with $q > 0.4 k_L$ we obtain an integrated Berry phase that suggests an asymptotic Chern number of $\Phi_B/2\pi = 0.01(1)$ for the non-topological branch and $\Phi_B/2\pi = 0.5(5)$ for the topological branch. However, Berry's phase measurements including ours includes the (potential) contribution of any Dirac strings traversing the integration area. In our system, these are possible at the Dirac point *, and each contributes $\pm 2\pi$ to Φ_B as was discussed in Section ???. Even with this 2π ambiguity we are able to associate a half-integer Chern number with the topological branch, which is possible only for a topological dispersion branch in the continuum.

8.6 Conclusion

In conventional lattices — for example graphene, or the topological Haldane model — it is well established that Dirac points each contribute a Berry's phase of $\Phi_B/2\pi = \pm 1/2$ [28], but crystalline materials conspire for these to appear in

pairs [29], always delivering integer Chern numbers. In contrast, our continuum system contains a single Dirac point, resulting in a non-integer Chern number. This leads to intriguing questions about edge states at interfaces with non-integer Chern numbers with non-integer Chern number differences. Initial studies in the context of electromagnetic waveguides [30] and atmospheric waves [31] have applied Chern invariants and the bulk-edge correspondence to continuous media.

While the true Rashba Hamiltonian features a ring of degenerate eigenstates, our implementation including the quadratic and cubic Dresselhaus-like SOC lifts this macroscopic degeneracy giving three nearly degenerate minima [15]. Already these three minima could allow the study of rich ground state physics in many body systems of bosons, for example the formation of fragmented BECs [10] when the system does not condense into a single-particle state. Furthermore, the use of additional spin states or larger Raman couplings can partially restore this degeneracy allowing the possible realization of fractional Hall like states [32].

Appendix A: The good, the bad and the ugly of RbLi

This appendix summarizes the best, the worst and the meh aspects of the RbLi apparatus. Hopefully the items presented here are helpful to future students building experimental apparatuses for ultracold atoms.

A.1 The good

It is very easy to come up with a list of bad things that don't work quite well in the lab. Coming up with a list of good things that work well is harder; if we are not fixing a broken thing we don't think much about it. When the current postdoc was prompted with the question of what she loved most about our apparatus she answered 'I love every single thing about RbLi.' Unfortunately there is not enough space to talk about every single thing and the list below summarizes some good things in our lab.

Overkill transistor banks: Large currents in the lab (quadrupole and Zeeman slower) are controlled with MOSFET banks formed by a group of MOSFETS whose drain and source are connected in parallel and sharing the same gate voltage that is controlled by a PI servo. The Zeeman slower always operates at a fixed current but the current in the quadrupole coils is dynamically changed throughout

the experimental sequence and a fast response is desirable. In 2013 we replaced the quadrupole MOSFET bank with a new unit that contains 20 IXFN 520N075T2 transistors rated for 75 V and 480 A (left panel of Figure 1). Even though our currents never exceed 70 A, the performance of the transistors really decays as the drain to source voltage is increased as can be seen in the right panel of Figure 1. The use of more transistors reduces the power dissipation of each individual transistor which allows us to operate the power supply at a higher voltage of 15 V that helps counteract the inductive kickback of the coils. With the new transistor bank the turn on time of the coils was reduced from 100 ms to 50 ms leading to improved magnetic trapping and better Stern-Gerlach pulses for imaging, only with an unavoidable small number of blown off transistors.

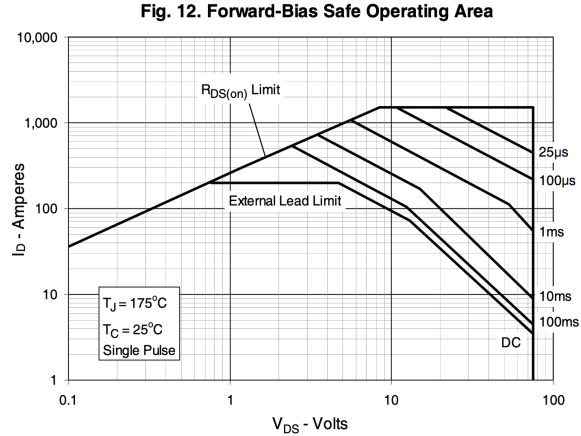
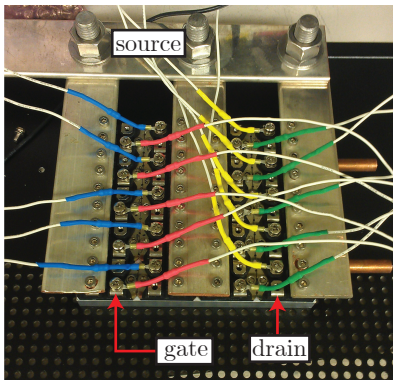


Figure 1: Left: New MOSFET bank. Right: Safe operation regime of the IXFN 520N075T2 MOSFET. Even though they are in principle rated for up to 480 A the maximum safe current is greatly reduced at larger drain to source voltages V_{DS} . A high V_{DS} is desirable to reduce the inductive kickback during turn on.

Hand made in vacuum shutters: Before going into the Zeeman slower, the atoms that were heated in the Rb oven travel to the main oven chamber that is

pictured in Figure 2b containing a cold-cup and an oven shutter. The cold-cup is a cylindrical shaped copper piece that is attached to the cold end of a thermo-electric cooler (TEC) via a copper rod. We keep the cold-cup temperature at -30 C in order to capture excess Rb atoms in the chamber and prevent damaging the ion pumps. The oven shutter allows us to block after the MOT loading stage to prevent unwanted heating. We use a homemade device, made from a re-purposed hard drive disk shutter with a metallic flag attached to its end. The shutter is electrically connected to an electric feedthrough with vacuum-compatible Kapton sealed wires. Other apparatus within the JQI [33] have commercial shutters from **Uniblitz** and some of them have failed in the past. Overall we have found this setup to be very reliable. The only problem we experienced once was some accumulation of Rb on the cold cup that started blocking the atomic beam. To remedy this we reversed the polarity of the TEC and heated the cold cup barely enough so that the accumulated Rb atoms melted and moved away from the aperture of the atomic beam.

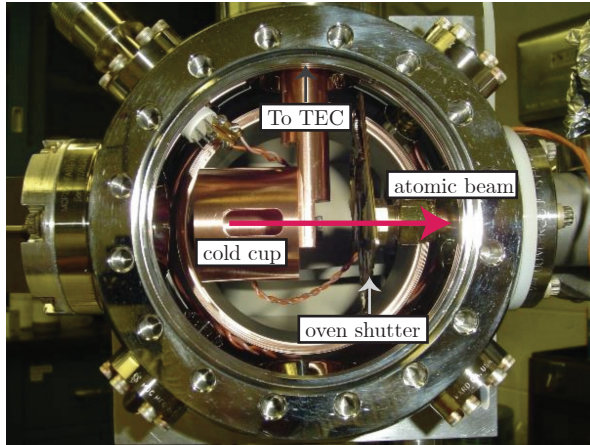


Figure 2: The RbLi oven chamber. We use a homemade in-vacuum shutter to block the atomic beam after the MOT stage to prevent heating of the atoms at later stages.

Ultraviolet LEDs: We have two 3 W ultraviolet LEDs from **Mightex** placed at the glass cell side of the vacuum system. One is aimed at the vacuum window where the slower beam enters and the other is placed aiming at the glass cell. The LEDs prevent Rubidium from depositing on the vacuum system and can conveniently be turned on and off with a TTL signal from the computer. We have found that routinely turning them on (for example, leaving them on overnight) leads to a smoother operation of the system.

Mirror mounts with picomotor actuators: We use 8816-6 picomotor optical mounts from **New Focus Optics** whose deflection angle can be electronically adjusted on the order of microradians. The addition of picomotor mounts has made alignment of laser beams to the atoms significantly easier. We use this mounts on the last tunable mirror before the atoms for beam paths whose alignment is critical, for example in optical dipole trap and Raman beams.

Polarizers on MOT beams: The light of our MOT beams is coupled to polarization maintaining optical fibers. We found that besides our best efforts to align the polarization of the incoming light to the axis of the fiber the fluctuations in the output polarization could cause considerable instabilities in the BEC production. To keep the polarization clean we placed polarizers at the output of the fibers. We found that despite the power hit we can get from the changes in polarization, this solution leads to a much more stable production of BECs.

Lab couch: When the experiment is functional enough that data can be taken long hours in the lab are often required. If it gets late, the lab couch allows the person running the experiment to take small naps as the data keeps coming while

still being close to the apparatus in case something needs to be fixed.

Other elements already mentioned in the main text: The new master laser from Vescent photonics has been very stable and reliable. The new Mako camera has been very helpful to get rid of unwanted fringes in absorption images. Labscript makes writing experimental sequences very straightforward.

A.2 The bad

The bad, these are elements of the apparatus that were constant sources of pain and if considering a new experimental design should be avoided.

Water cooling shared between two labs: The quadrupole and Zeeman slower coils as well as the transistor banks require water cooling due to Joule heating. Our lab space is shared with a Rubidium-Ytterbium ultracold mixtures apparatus [34] and amongst the things we shared is the water cooling system. The schematic in Figure 3 illustrates the layout of the water cooling system. The water was filtered at two different points, first at each line has a $440\ \mu\text{m}$ particulate filter from **Swagelok** and then the water returning to the heat exchanger is filtered with a low-impedance cellulose cartridge (**McMaster** 7191K11). Both filters only capture impurities in the water for one given flow direction. One of the failure modes which occurs when one of the booster pumps is turned on before the heat exchanger, causing water to flow from one experiment to the other and bringing a collection of nasty things that escapes the filters into the coils. Over the years our system has suffered of clogged filters, clogged coils and broken booster pumps. For best operation it

is highly recommended that the cartridge filter is changed and that the Swagelok filters be cleaned at least once a year and that a 10% solution of an anti-corrosive Optishield Plus in water is used as a coolant. Even when following this practices, we managed to find lots of gunk and unidentified objects (sand? glass? mud? oxide? dead bacteria?) in the water, just at a slower rate.

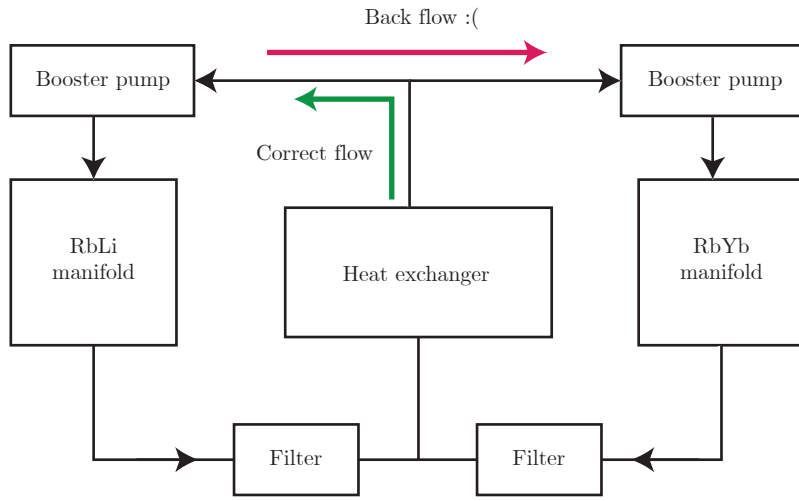


Figure 3: Simplified schematic of the shared water cooling manifold.

Flipper mirrors: The optical path of the MOT beams near the atoms is very close to that of Raman, optical dipole trap and probe beams. Since the MOT beams are only used at the early stages of the experiment it is tempting to use flipper mirror mounts so that once they are no longer needed they can be moved away to make space for other beams. This was the approach originally taken in the lab and we used 8893-K motorized optical flipper mounts from Newport in multiple locations. As they break over and over again, they have been slowly replaced by more stable solutions such as periscopes or polarizing beam splitters wherever it is

possible. Flipper mirrors are always bound to break, it is only a matter of time.

Avoid using them unless you absolutely have no alternative.

Optical fibers right below air vents: The optical fibers connecting the main experiment optical table and the laser optical table are routed close to a pair of AC vents in the lab. The changes in air temperature result in polarization fluctuations at the output of optical fibers, a constant cause of pain and instability in our BEC production. We have tried to remedy this issue by partially blocking vents and enclosing the fibers in a large PVC tube.

Free space dipole laser: The laser system providing 1064 nm light for the optical dipole trap is not fiber coupled and is setup in the same optical table as the vacuum system; we are not able to change the laser without destroying the alignment of the beam with the atoms. This issue became important while setting up a 1D optical lattice by retro-reflecting one of the dipole trap beams we noticed that the laser mode is not very stable, leading to big fluctuations in the optical lattice. In the original design of the laser system high-power photonic crystal fibers were included but they did not have built in mode expanders which resulted in the tip of the fiber inevitably getting burnt after some time of use. In short, mode expanders are recommended in applications involving large optical powers.

A.3 The ugly

The ugly elements are not quite bad but they don't function flawlessly either. If given the option to replace them with something better I definitely would.

Kepco bipolar power supplies: We use three Kepco BOP 20-20M bipolar power supplies to provide the current for the bias coils. While it is nice to have a commercially available power supply that can provide $\pm 20\text{ A}$ they come with a few drawbacks. First the current they provide has 60 Hz noise in it and in order to suppress it and stabilize the currents we must use a PI feedback circuit. The power supplies has multiple banks of NPN and PNP transistors inside mounted on a big heat sink with fans attached to it making them quite noisy; it is not optimal to place them close to the main experiment chamber and long connections open the door to unwanted ground loops. Additionally they have a few failure modes. The most common problem we experienced was output current would rail, which is related to broken transistors which tend to inevitably fail after some time. Many of the symptoms of broken Kepcos spoken by other labs seem to usually boil down to malfunctioning transistors.

Toptica's BoosTA: Our cooling light comes from a Toptica DL Pro is amplified using a Toptica BoosTA tapered amplifier system. While the output power of this TA has been relatively stable over the years it has a tendency to turn itself off. On its bad days it would turn off so often that it would be impossible to operate the experiment. We haven't been able to identify the problem despite our best efforts to look into the TA controller, the TA itself, multiple conversations with Toptica engineers etc.

Too many devices connected to the same computer: We use multiple USB-6229 data acquisition (DAQ) devices from National Instruments. They are located at different points of the lab and then connected to the control computer

through USB to optical fiber adapters that break the ground between the computer and the rest of the lab equipment (a practice we always try to follow when connecting things to the computer). We have a total of 6 NI devices in addition to other equipment like oscilloscopes all connected to the computer through BNC cables. Often times we struggled with the computer failing to detect one or multiple devices and it would take a very special (and different every time) combination of plugging and unplugging, turning off and turning back on things until all devices were recognized by the computer. We observe that the problem occurs less often when we don't have as many USB devices connected to the computer.

Appendix B: New apparatus

As mentioned in the main text, the construction of a new apparatus for producing BECs of ^{87}Rb and ^{39}K is underway. The design of the apparatus is intended to be a bug fix version of the RbChip [35] lab at NIST. The new apparatus does not have a Zeeman slower and instead will use magnetic transport coils to move atoms from a MOT cell to the main science cell.

This Appendix describes some aspects of the design and construction of the new apparatus where I was involved. Disclaimer: none of this things have been tested yet so we don't know yet if it will all work horribly. I have listed all relevant part numbers in case replacements are needed.

B.1 Water cooling

The lack of a Zeeman slower in the apparatus greatly simplifies the water cooling system compared to that of RbLi. Since we don't anticipate to have any coils with high flow impedance we expect that the pressure from a recirculating chiller will be enough to provide water cooling to the transistor banks and the magnetic transport coils.

Our choice of chiller was the TF1LN400-LN 1.4 kW recirculating chiller from

Thermo Fisher Scientific. The water is filtered both at the output and the return with a high-impedance filter with a cellulose cartridge (filter: McMaster 4422K3, cartridge: McMaster 7191K11). A breakout manifold divides the chilled water into 5 different lines, each one with a flow meter (Proteus Industries 0101C110) that can be used to interlock the current of water cooled applications to the flow of water. Based on previous experiences with plumbing (see Appendix A) I highly encourage replacing the filters at least once a year and to use a solution of 10% corrosion inhibitor (e.g. OptiShield Plus) and distilled water as a coolant.

a. Service corridor side



b. Experiment side

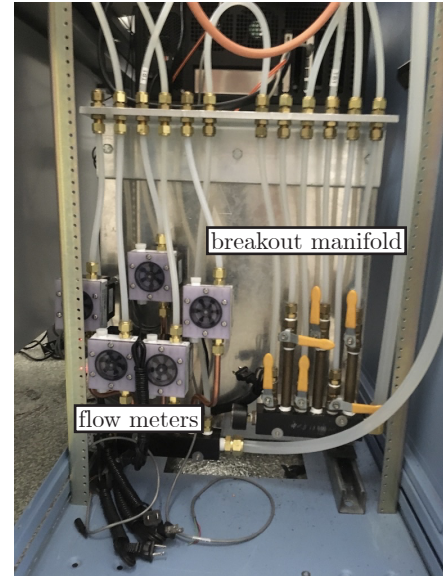


Figure 1: Water cooling

B.2 Electrical installation

We have two Agilent 6690A (440 A at 15 V max. current) to provide all the necessary currents. The power supplies are located in the service corridor and are

connected to three copper bars corresponding to $\pm 15\text{ V}$ and ground using welding cable (McMaster 7818A17) that is laid on cable trays (McMaster 30065T11 e.g.). The cables are arranged in the pattern shown in Figure xxx so that the magnetic field produced by them is closer to a magnetic quadrupole which decays faster than the field of a magnetic dipole. We are not planning to use commercial bipolar power supplies in this lab (see Appendix A) and instead we will be using a MOSFET based homemade device that will draw current from the $\pm 15\text{ V}$ rails.

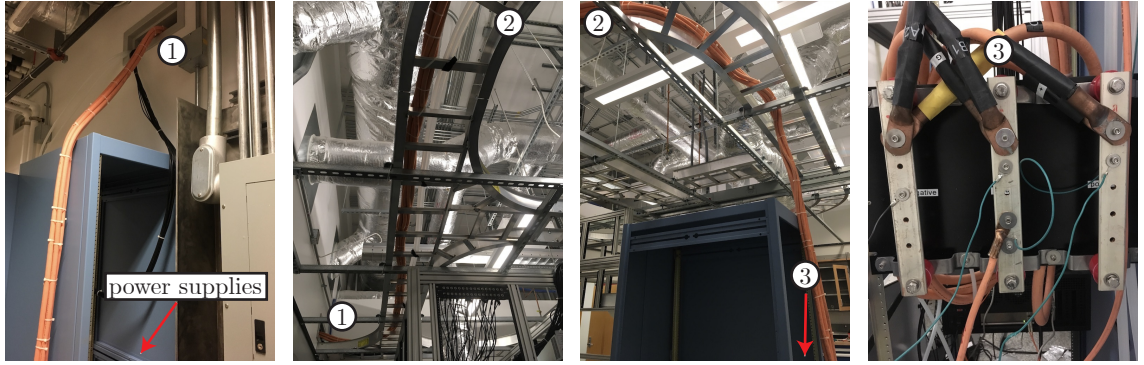


Figure 2: A roller coaster ride, from the power supplies in the service corridor to three copper bars that distribute the power.

B.3 Coil winding

All the coils in the apparatus including magnetic transport, bias and gradient cancellation have been wound using Laminax ribbon wire from Bridgeport Magnetics. We followed the coil fabrication process described in [35] which involves first winding a fixed number of turns around a prefabricated form with a particular geometry. The coils were then covered with a machinable epoxy (Stycast 1266) to fill in any air gaps. A lesson we learned while doing this is that only room

temperature epoxy should be mixed. We keep the epoxy in a fridge to extend its lifetime but if it is cold some tiny drops of water will condense in it as it is being mixed and it will not properly be cured. To minimize the air bubbles we placed the coils with epoxy on a vacuum bell and we pumped the air out using an electric vacuum pump ([McMaster 4396K21](#)). After the epoxy has cured (overnight if it is left at room temperature or less if it is left at higher temperature) the coils are ready for lathing to remove all excess epoxy and kapton tape up to the surface of the copper. After some trial and error (and lots of frustration) we found that using a diamond tip cutter ([McMaster 3316A32](#)) and spinning the lathe not faster than 150 rpm the best results. Using a cutter that is not sharp enough or cutting too aggressively close to the soft copper results in deformed rather. In the past when coils were fabricated at NIST a lathing form was used to mount the coils on the lathe. The machinist at UMD considered this was not safe enough so I instead mounted the coils using a 6 jaw chuck as shown in Figure 3a. than cut traces that merge into each other causing unwanted shorts. For anyone making coils in the future: it is sort of an art to get it right and screwing up many coils is part of learning the art.

B.4 Rb source and ‘oven’

The Rb source consists of a 1.33” CF flanged bellow ([Kurt J. Lesker MH-CF-A03](#)) with a Rb ampule . The bellow is housed in a cold ‘oven’ which is designed to keep the source at a temperature $\approx 1\text{ C}$ to keep the vapor pressure low. The oven is made of hollow aluminum cylinder with a slit on one side with tapped holes so that

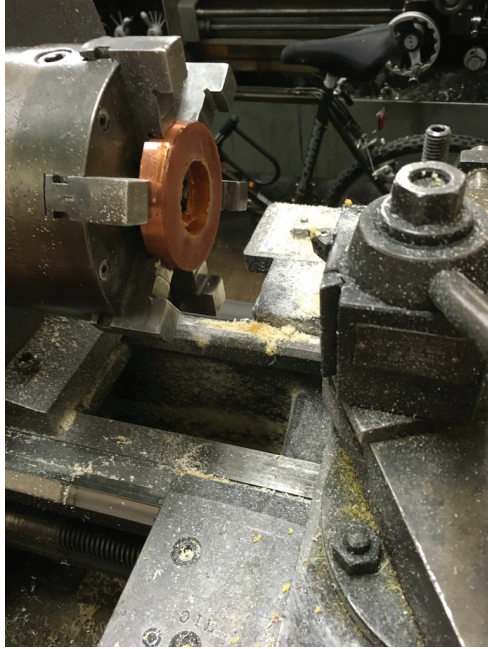


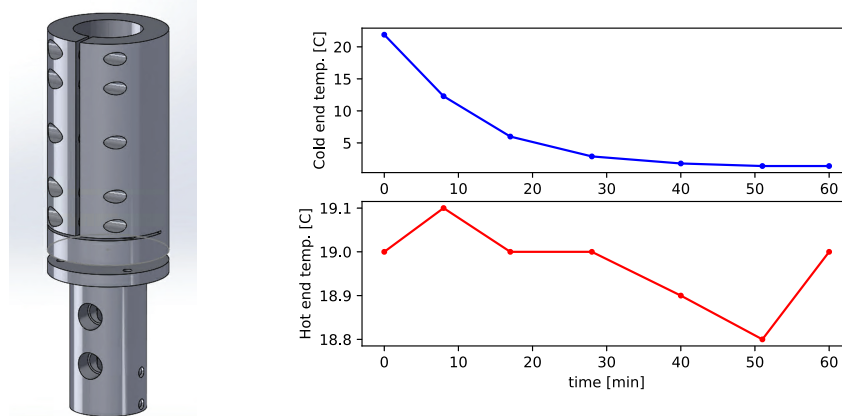
Figure 3: A roller coaster ride, from the power supplies in the service corridor to three copper bars that distribute the power.

1/4 – 20 screws can be used to fix the oven to the source. The bottom of the oven attaches to the cold end of a TEC that provides the cooling. The hot side of the TEC is attached to a heat sink made of a hollow brass piece with tapped holes for 1/4” NPT pipes are used to provide water cooling. The left panel of Figure xxx shows CAD drawings of the oven both of this parts and the right panel shows the actual parts mounted on a test bench. The Rb source will be connected to the MOT glass cell; the plan is to use light induced atomic desorption (LIAD) [36] to increase the Rb vapor pressure for MOT loading using non-thermal means.

Our initial hope was to control the temperature using a linear temperature controller designed at the JQI (the design is available at the [JQI GitHub](#)) inter-

faced to the lab computer and Labscript using a serial to ethernet adapter (WIZnet WIZ107SR). Unfortunately this project is not completed to this date.

a. Rb ‘oven’ and heat sink b. Bench test temperatures



c. Testing prototype oven and heat sink

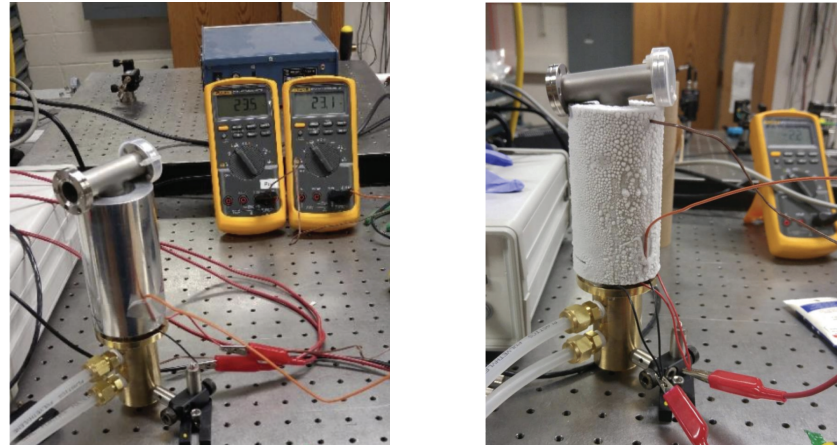


Figure 4: Rubidium oven assembly

B.5 Table enclosures

The enclosures of the optical tables are made of **Alumalite** from **Laminators Inc.** mounted on frames made out of aluminum extrusions from 80/20 and sliding tracks (2220 and 2210). Alumalite is a sandwich of a corrugated polypropylene material in between two thin sheets of aluminum. We chose this ma-

terial because it is strong and lightweight. Its laser safety properties remain to be tested but we anticipate it is better than the acrylic panels at the RbLi lab. The initial frames were designed and built mostly by former graduate student Daniel Campbell and later finished and modified by former undergraduate student Eliot Fenton and me.

To the new and future members of the lab: I sincerely hope the things I designed and built don't cause you much pain!

Appendix C: Full derivation of the Raman coupled $|xyz\rangle$ states

In this Appendix I derive the full time-dependent Hamiltonian describing the $|xyz\rangle$ states coupled by three Raman beams as shown in Figure 1. The system is based on the theoretical proposal in [17] to engineer a system with Rashba-like SOC.

We consider ^{87}Rb atoms in the ground hyperfine $F = 1$ manifold subject to a constant magnetic field $B_0\mathbf{e}_z$ and an RF magnetic field $B_{\text{RF}} \cos(\omega_{\text{RF}}t)\mathbf{e}_x$ as in Chapter ???. The system is described by the Hamiltonian

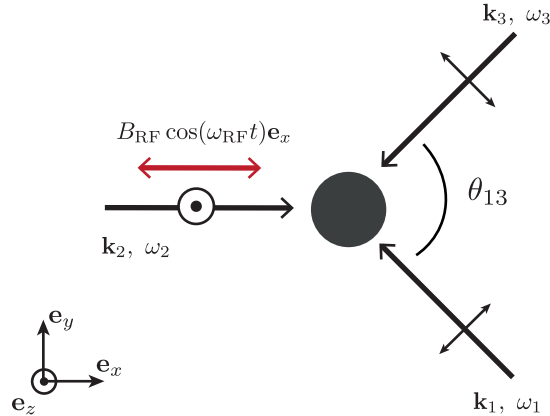


Figure 1: Laser layout: We use a strong RF field and three linearly polarized Raman beams propagating in the xy plane couple the $|xyz\rangle$ states and engineer the Rashba Hamiltonian.

$$\hat{H}_{\text{RF}} = \omega_0 \hat{F}_z - \frac{\epsilon}{\hbar} (\hat{F}_z^2 - \mathbb{I}) + 2\Omega_{\text{RF}} \cos(\omega_{\text{RF}}t) \hat{F}_x, \quad (\text{C.1})$$

where $\omega_0 = g_F\mu_B B_0$ is the Larmor frequency, ϵ is a quadratic Zeeman shift that breaks the degeneracy of the $|m_F = -1\rangle \leftrightarrow |m_F = 0\rangle$ and $|m_F = 1\rangle \leftrightarrow |m_F = 0\rangle$ transitions, and $\Omega_{RF} = g_F\mu_B B_{RF}/2$ is the RF coupling strength. We transform the Hamiltonian into a rotating frame using the unitary transformation $\hat{U}(t) = \exp(-i\omega_{RF}t\hat{F}_z)$. The spin-1 operators under this transformation become

$$\begin{aligned}\hat{F}_x &\rightarrow \cos(\omega_{RF}t)\hat{F}_x - \sin(\omega_{RF}t)\hat{F}_y \\ &= e^{i\omega_{RF}t}\hat{F}_+ + e^{-i\omega_{RF}t}\hat{F}_- \\ \hat{F}_y &\rightarrow \sin(\omega_{RF}t)\hat{F}_x + \cos(\omega_{RF}t)\hat{F}_y \\ &= \frac{1}{i}(e^{i\omega_{RF}t}\hat{F}_+ - e^{-i\omega_{RF}t}\hat{F}_-) \\ \hat{F}_z &\rightarrow \hat{F}_z.\end{aligned}\tag{C.2}$$

The unitary evolution in the rotating frame is described by the transformed Hamiltonian $\hat{U}^\dagger(t)(\hat{H}_{RF} - i\hbar\partial_t)\hat{U}(t)$, which after neglecting terms that are oscillating with angular frequency $2\omega_{RF}$ is

$$\hat{H}_{RWA} = \Delta\hat{F}_z - \frac{\epsilon}{\hbar}(\hat{F}_z^2 - \mathbb{I}) + \Omega_{RF}\hat{F}_x\tag{C.3}$$

The eigenstate of Equation C.3 are the $|xyz\rangle$ states described in Chapter ??.

For simplicity I first describe the Raman coupling in the lab frame and I consider the geometry and polarization of the Raman beams as in Figure 1. The

electric field at the atoms is

$$\mathbf{E}(x, t) = \sum_{i=1}^3 E_i \mathbf{e}_i e^{i(\mathbf{k}_i \cdot \mathbf{x} - \omega_i t)}, \quad (\text{C.4})$$

where E_i is the field amplitude, ω_i is the angular frequency, \mathbf{k}_i is the wave vector and \mathbf{e}_i is the polarization of each of the beams. In order to have the right coupling matrix elements to cyclically couple all three states in a ring-like coupling as described in [15] we need non-zero transition matrix elements we need a Hamiltonian of the form

$$\hat{H}_{\text{SOC}} = (\Omega_x, \Omega_y, \Omega_z) \cdot \hat{\mathbf{F}} \quad (\text{C.5})$$

(see Section ??). I show that this is possible if we choose two Raman beams to have in plane polarization and one vertically polarized beam:

$$\begin{aligned} \mathbf{e}_1 &= \frac{(k_{1y}, -k_{1x}, 0)}{\|\mathbf{k}_1\|^2}, \\ \mathbf{e}_2 &= (0, 0, 1), \\ \mathbf{e}_3 &= \frac{(k_{3y}, -k_{3x}, 0)}{\|\mathbf{k}_3\|^2}, \end{aligned} \quad (\text{C.6})$$

The Raman coupling strength is proportional to the vector polarizability (see Section ??) and the Hamiltonian describing the atom-light coupling is

$$\hat{H}_R = (i u_v \mathbf{E} \times \mathbf{E}^*) \cdot \hat{\mathbf{F}}, \quad (\text{C.7})$$

where u_v is the vector polarizability. The expression for the cross product of the electric field at the atoms is quite messy, lets rewrite it in a more convenient way:

$$\begin{aligned}
\mathbf{E} \times \mathbf{E}^* &= (E_1^* \mathbf{e}_1 e^{-i(\mathbf{k}_1 \cdot \mathbf{x} - \omega_1 t)} + E_2^* \mathbf{e}_2 e^{-i(\mathbf{k}_2 \cdot \mathbf{x} - \omega_2 t)} + E_3^* \mathbf{e}_3 e^{-i(\mathbf{k}_3 \cdot \mathbf{x} - \omega_3 t)}) \times c.c \\
&= E_1^* E_2 (\mathbf{e}_1 \times \mathbf{e}_2) e^{i[(\mathbf{k}_2 - \mathbf{k}_1) \cdot \mathbf{x} - (\omega_2 - \omega_1)t]} + E_1^* E_3 (\mathbf{e}_1 \times \mathbf{e}_3) e^{i[(\mathbf{k}_3 - \mathbf{k}_1) \cdot \mathbf{x} - (\omega_3 - \omega_1)t]} \\
&\quad + E_2^* E_1 (\mathbf{e}_2 \times \mathbf{e}_1) e^{i[(\mathbf{k}_1 - \mathbf{k}_2) \cdot \mathbf{x} - (\omega_1 - \omega_2)t]} + E_2^* E_3 (\mathbf{e}_2 \times \mathbf{e}_3) e^{i[(\mathbf{k}_3 - \mathbf{k}_2) \cdot \mathbf{x} - (\omega_3 - \omega_2)t]} \\
&\quad + E_3^* E_1 (\mathbf{e}_3 \times \mathbf{e}_1) e^{i[(\mathbf{k}_1 - \mathbf{k}_3) \cdot \mathbf{x} - (\omega_1 - \omega_3)t]} + E_3^* E_2 (\mathbf{e}_3 \times \mathbf{e}_2) e^{i[(\mathbf{k}_2 - \mathbf{k}_3) \cdot \mathbf{x} - (\omega_2 - \omega_3)t]} \\
&= 2i \left[(\mathbf{e}_1 \times \mathbf{e}_2) \text{Im}\{E_1^* E_2 e^{i(\mathbf{k}_{21} \cdot \mathbf{x} - \omega_{21} t)}\} \right. \\
&\quad + (\mathbf{e}_1 \times \mathbf{e}_3) \text{Im}\{E_1^* E_3 e^{i(\mathbf{k}_{32} \cdot \mathbf{x} - \omega_{32} t)}\} \\
&\quad \left. + (\mathbf{e}_2 \times \mathbf{e}_3) \text{Im}\{E_2^* E_3 e^{i(\mathbf{k}_{32} \cdot \mathbf{x} - \omega_{32} t)}\} \right] \\
\end{aligned} \tag{C.8}$$

and using the definition of the polarization vectors (Equation C.6)

$$\begin{aligned}
\mathbf{e}_1 \times \mathbf{e}_2 &= \frac{(-k_{1x}, -k_{1y}, 0)}{\|\mathbf{k}_1\|^2} = -\hat{\mathbf{k}}_1 \\
\mathbf{e}_1 \times \mathbf{e}_3 &= \frac{(0, 0, -k_{1y}k_{3x} + k_{3y}k_{1x})}{\|\mathbf{k}_1\|^2 \|\mathbf{k}_3\|^2} = \mathbf{e}_z \sin \theta_{13} \\
\mathbf{e}_2 \times \mathbf{e}_3 &= \frac{(k_{3x}, k_{3y}, 0)}{\|\mathbf{k}_3\|^2} = \hat{\mathbf{k}}_3,
\end{aligned} \tag{C.9}$$

we obtain the Hamiltonian describing the atom light interaction

$$\begin{aligned}
iu_v \mathbf{E}^* \times \mathbf{E} \cdot \hat{\mathbf{F}} &= -2u_v \left[-\hat{\mathbf{k}}_1 \text{Im}\{12\} + \mathbf{e}_z \sin \theta_{13} \text{Im}\{13\} + \hat{\mathbf{k}}_3 \text{Im}\{23\} \right] \cdot \hat{\mathbf{F}} \\
&= (\Omega_x, \Omega_y, \Omega_z) \cdot \hat{\mathbf{F}},
\end{aligned} \tag{C.10}$$

where

$$\begin{aligned}\Omega_x &= \frac{k_{1x}}{\|\mathbf{k}_1\|} \text{Im}\{\Omega_{12} e^{i(\mathbf{k}_{21} \cdot \mathbf{x} - \omega_{21} t)}\} + \frac{k_{3x}}{\|\mathbf{k}_3\|} \text{Im}\{\Omega_{23} e^{i(\mathbf{k}_{32} \cdot \mathbf{x} - \omega_{32} t)}\} \\ \Omega_y &= \frac{k_{1y}}{\|\mathbf{k}_1\|} \text{Im}\{\Omega_{12} e^{i(\mathbf{k}_{21} \cdot \mathbf{x} - \omega_{21} t)}\} + \frac{k_{3y}}{\|\mathbf{k}_3\|} \text{Im}\{\Omega_{23} e^{i(\mathbf{k}_{32} \cdot \mathbf{x} - \omega_{32} t)}\} \\ \Omega_z &= \text{Im}\{\Omega_{13} e^{i(\mathbf{k}_{31} \cdot \mathbf{x} - \omega_{31} t)}\},\end{aligned}\quad (\text{C.11})$$

and

$$\begin{aligned}\Omega_{12} &= 2u_v E_1^* E_2 \\ \Omega_{13} &= -2u_v E_1^* E_3 \sin \theta_{13} \\ \Omega_{23} &= -2u_v E_2^* E_3.\end{aligned}\quad (\text{C.12})$$

C.0.0.1 Going into rotating frame

This is where things start getting fun. We need to transform Eq. C.10 into the rotating frame. Which terms are ‘slow’ and we get to keep and which are ‘fast’ depends on the specific choice of Raman frequencies. The frequencies of the beams should be such that each of the frequency differences ω_{ij} is resonant with a dressed state transition in the rotating frame as shown in Figure 2a. I showed in Equation C.2 that in the rotating frame the \hat{F}_x and \hat{F}_y operators get additional factors of $\exp(\pm i\omega_{\text{RF}})$ while \hat{F}_z remains unchanged.

We must therefore have the frequencies of beams giving rise to \hat{F}_x and \hat{F}_y coupling to differ in frequency by an additional ω_{RF} and the beams that give the \hat{F}_z coupling to be close in frequency. The two possible ways of doing so are shown in

Figure 2b and they determine whether ω_{21} and ω_{31} are positive or negative.

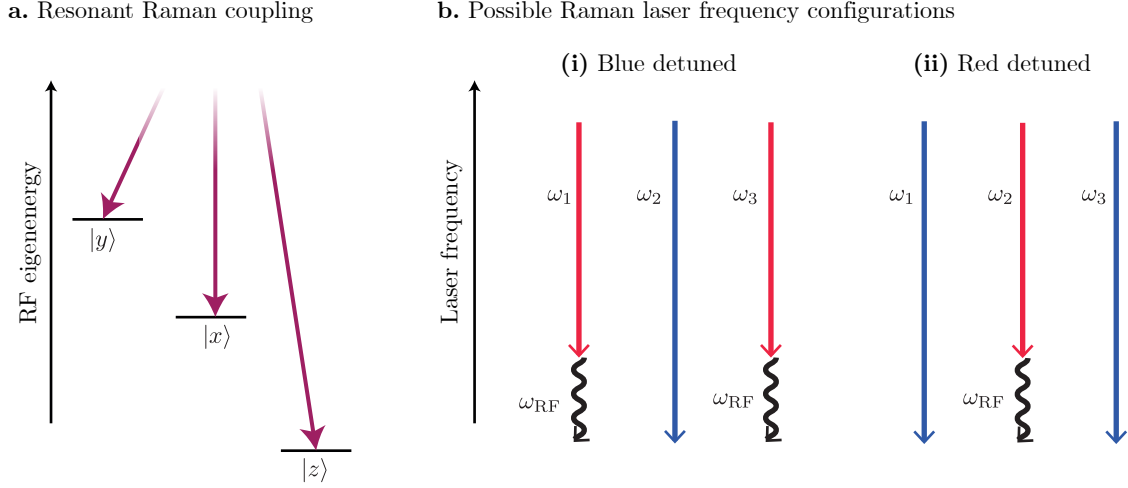


Figure 2: **a** The choice of laser frequencies should be such that in the frame rotating with frequency ω_{RF} we get resonant Raman coupling of the $|xyz\rangle$ states. **b**. Possible laser frequency configurations: **i)** Blue detuned configuration: There are 2 frequencies smaller by about ω_{RF} and one larger frequency. **ii)** The red detuned configuration: there are 2 frequencies that are larger by about ω_{RF} and one smaller frequency.

Lets look at the first term of the $\Omega_x \hat{F}_x$ coupling to get an idea of how the RWA will work here:

$$\begin{aligned}
\Omega_x^{(1)} \hat{F}_x &\rightarrow \frac{1}{4i} \frac{k_{1x}}{\|\mathbf{k}_1\|} \left(\Omega_{12} e^{i(\mathbf{k}_{21} \cdot \mathbf{x} - \omega_{21})t} - \Omega_{12}^* e^{-i(\mathbf{k}_{21} \cdot \mathbf{x} - \omega_{21}t)} \right) \left(e^{i\omega_{RF}t} \hat{F}_+ + e^{-i\omega_{RF}t} \hat{F}_- \right) \\
&\approx \frac{1}{4i} \frac{k_{1x}}{\|\mathbf{k}_1\|} \left(\Omega_{12} e^{i(\mathbf{k}_{21} \cdot \mathbf{x} - (\omega_{21} \mp \omega_{RF})t)} \hat{F}_\pm - \Omega_{12}^* e^{-i(\mathbf{k}_{21} \cdot \mathbf{x} - (\omega_{21} \mp \omega_{RF})t)} \hat{F}_\mp \right) \\
&= \frac{1}{2} \frac{k_{1x}}{\|\mathbf{k}_1\|} |\Omega_{12}| \left(\sin[\mathbf{k}_{21} \cdot \mathbf{x} - (\omega_{21} \mp \omega_{RF})t + \phi_{12}] \hat{F}_x \right. \\
&\quad \left. \pm \cos[\mathbf{k}_{21} \cdot \mathbf{x} - (\omega_{21} \mp \omega_{RF})t + \phi_{12}] \hat{F}_y \right).
\end{aligned} \tag{C.13}$$

Here the upper sign corresponds to the $\omega_{21} > 0$ case (blue detuned) and the lower

sign to $\omega_{21} < 0$ (red detuned) and I performed a RWA approximation in the second line by neglecting the terms oscillating with frequency close to $2\omega_{\text{RF}}$. Similarly, the second therm of $\Omega_x \hat{F}_x$ is

$$\begin{aligned}
\Omega_x^{(2)} \hat{F}_x &\rightarrow \frac{1}{4i} \frac{k_{3x}}{\|\mathbf{k}_3\|} (\Omega_{23} e^{i(\mathbf{k}_{32} \cdot \mathbf{x} - \omega_{32})t} - \Omega_{23}^* e^{-i(\mathbf{k}_{32} \cdot \mathbf{x} - \omega_{32}t)}) (e^{i\omega_{\text{RF}}t} \hat{F}_+ + e^{-i\omega_{\text{RF}}t} \hat{F}_-) \\
&\approx \frac{1}{2} \frac{k_{3x}}{\|\mathbf{k}_3\|} |\Omega_{23}| \left(\sin[\mathbf{k}_{32} \cdot \mathbf{x} - (\omega_{32} \mp \omega_{\text{RF}})t + \phi_{23}] \hat{F}_x \right. \\
&\quad \left. \pm \cos[\mathbf{k}_{32} \cdot \mathbf{x} - (\omega_{32} \mp \omega_{\text{RF}})t + \phi_{23}] \hat{F}_y \right)
\end{aligned} \tag{C.14}$$

where I used the same sign convention as before. It is important to keep in mind that if ω_{21} is positive then ω_{32} must be negative and vice versa. Lets keep cranking the algebra!

$$\begin{aligned}
\Omega_y^{(1)} \hat{F}_y &\rightarrow -\frac{1}{4} \frac{k_{1y}}{\|\mathbf{k}_1\|} (\Omega_{12} e^{i(\mathbf{k}_{21} \cdot \mathbf{x} - \omega_{21}t)} - \Omega_{12}^* e^{-i(\mathbf{k}_{21} \cdot \mathbf{x} - \omega_{21}t)}) (e^{i\omega_{\text{RF}}t} \hat{F}_+ - e^{-i\omega_{\text{RF}}t} \hat{F}_-) \\
&\approx \mp \frac{1}{4} \frac{k_{1y}}{\|\mathbf{k}_1\|} (\Omega_{12} e^{i(\mathbf{k}_{21} \cdot \mathbf{x} - (\omega_{21} \mp \omega_{\text{RF}})t)} \hat{F}_\pm + \Omega_{12}^* e^{-i(\mathbf{k}_{21} \cdot \mathbf{x} - (\omega_{21} \mp \omega_{\text{RF}})t)} \hat{F}_\mp) \\
&= \mp \frac{1}{2} \frac{k_{1y}}{\|\mathbf{k}_1\|} |\Omega_{12}| \left(\cos[\mathbf{k}_{21} \cdot \mathbf{x} - (\omega_{21} \mp \omega_{\text{RF}})t + \phi_{12}] \hat{F}_x \right. \\
&\quad \left. - \sin[\mathbf{k}_{21} \cdot \mathbf{x} - (\omega_{21} \mp \omega_{\text{RF}})t + \phi_{12}] \hat{F}_y \right),
\end{aligned} \tag{C.15}$$

$$\begin{aligned}
\Omega_y^{(2)} \hat{F}_y &\rightarrow -\frac{1}{4} \frac{k_{3y}}{\|\mathbf{k}_3\|} \left(\Omega_{23} e^{i(\mathbf{k}_{32} \cdot \mathbf{x} - \omega_{32} t)} - \Omega_{23}^* e^{-i(\mathbf{k}_{32} \cdot \mathbf{x} - \omega_{32} t)} \right) \left(e^{i\omega_{\text{RF}} t} \hat{F}_+ - e^{-i\omega_{\text{RF}} t} \hat{F}_- \right) \\
&\approx \mp \frac{1}{2} \frac{k_{3y}}{\|\mathbf{k}_3\|} |\Omega_{23}| \left(\cos[\mathbf{k}_{32} \cdot \mathbf{x} - (\omega_{32} \mp \omega_{\text{RF}})t + \phi_{23}] \hat{F}_x \right. \\
&\quad \left. - \sin[\mathbf{k}_{32} \cdot \mathbf{x} - (\omega_{32} \mp \omega_{\text{RF}})t + \phi_{23}] \hat{F}_y \right).
\end{aligned} \tag{C.16}$$

The complete Hamiltonian in the rotating frame after doing the rotating wave approximation is then

$$\begin{aligned}
\hat{H} = \frac{1}{2} \frac{|\Omega_{12}|}{\|\mathbf{k}_1\|} &\left(\left(k_{1x} \sin[\mathbf{k}_{21} \cdot \mathbf{x} - (\omega_{21} \mp \omega_{\text{RF}})t + \phi_{12}] \pm k_{1y} \cos[\mathbf{k}_{21} \cdot \mathbf{x} - (\omega_{21} \pm \omega_{\text{RF}})t + \phi_{12}] \right) \hat{F}_x \right. \\
&+ \left. \left(\pm k_{1x} \cos[\mathbf{k}_{21} \cdot \mathbf{x} - (\omega_{21} \mp \omega_{\text{RF}})t + \phi_{12}] \mp k_{1y} \sin[\mathbf{k}_{21} \cdot \mathbf{x} - (\omega_{21} \pm \omega_{\text{RF}})t + \phi_{12}] \right) \hat{F}_y \right) \\
\frac{1}{2} \frac{|\Omega_{23}|}{\|\mathbf{k}_3\|} &\left(\left(k_{3x} \sin[\mathbf{k}_{32} \cdot \mathbf{x} - (\omega_{32} \mp \omega_{\text{RF}})t + \phi_{23}] \pm k_{3y} \cos[\mathbf{k}_{32} \cdot \mathbf{x} - (\omega_{32} \pm \omega_{\text{RF}})t + \phi_{23}] \right) \hat{F}_x \right. \\
&+ \left. \left(\pm k_{3x} \cos[\mathbf{k}_{32} \cdot \mathbf{x} - (\omega_{32} \mp \omega_{\text{RF}})t + \phi_{23}] \mp k_{3y} \sin[\mathbf{k}_{32} \cdot \mathbf{x} - (\omega_{32} \pm \omega_{\text{RF}})t + \phi_{23}] \right) \hat{F}_y \right) \\
&+ |\Omega_{13}| \sin(\mathbf{k}_{31} \cdot \mathbf{x} - \omega_{31} t + \phi_{13}) \hat{F}_z
\end{aligned} \tag{C.17}$$

In order to go from this rather complicated looking Hamiltonian to the effective time independent Hamiltonian used in Chapter 8 we need to take two steps: first the off resonant coupling terms need to be neglected. This can be more or less safely done since they will be detuned by something on the order of tens to hundreds of kHz. Second we need to go into a second transformed frame using the unitary

transformation

$$\hat{U} = \sum_{i \in \{x, y, z\}} e^{i(\mathbf{k}_i \cdot \mathbf{x} - \omega_i t)} \quad (\text{C.18})$$

and eliminate the terms that are proportional to $\exp(i\omega_{ij})$. The neglected terms of the Hamiltonian in Equation C.17 have the effect of slightly shifting the eigenenergies of the effective Hamiltonian from Equation 8.8. We interpret this shifts in energy as coming from new effective Raman coupling strengths that slightly differ from our calibrations performed by measuring the Rabi frequencies of individual pairs of Raman beams.

Bibliography

- [1] Hirokazu Miyake, Georgios A. Siviloglou, Colin J. Kennedy, William Cody Burton, and Wolfgang Ketterle. Realizing the Harper Hamiltonian with Laser-Assisted Tunneling in Optical Lattices. *Physical Review Letters*, 111(18):185302, October 2013.
- [2] M. Aidelsburger, M. Atala, M. Lohse, J. T. Barreiro, B. Paredes, and I. Bloch. Realization of the Hofstadter Hamiltonian with Ultracold Atoms in Optical Lattices. *Physical Review Letters*, 111(18):185301, October 2013.
- [3] Gregor Jotzu, Michael Messer, Rémi Desbuquois, Martin Lebrat, Thomas Uehlinger, Daniel Greif, and Tilman Esslinger. Experimental realization of the topological Haldane model with ultracold fermions. *Nature*, 515(7526):237–240, November 2014.
- [4] H.-I Lu, M. Schemmer, L. M. Aycock, D. Genkina, S. Sugawa, and I. B. Spielman. Geometrical pumping with a bose-einstein condensate. *Phys. Rev. Lett.*, 116:200402, May 2016.
- [5] M. Lohse, C. Schweizer, O. Zilberberg, M. Aidelsburger, and I. Bloch. A Thouless quantum pump with ultracold bosonic atoms in an optical superlattice. *Nature Physics*, 12(4):350–354, April 2016.
- [6] Zhan Wu, Long Zhang, Wei Sun, Xiao-Tian Xu, Bao-Zong Wang, Si-Cong Ji, Youjin Deng, Shuai Chen, Xiong-Jun Liu, and Jian-Wei Pan. Realization of two-dimensional spin-orbit coupling for Bose-Einstein condensates. *Science*, 354(6308):83–88, October 2016.
- [7] Wei Sun, Bao-Zong Wang, Xiao-Tian Xu, Chang-Rui Yi, Long Zhang, Zhan Wu, Youjin Deng, Xiong-Jun Liu, Shuai Chen, and Jian-Wei Pan. Highly Controllable and Robust 2d Spin-Orbit Coupling for Quantum Gases. *Physical Review Letters*, 121(15):150401, October 2018.

- [8] Yu A. Bychkov and E. I. Rashba. Oscillatory effects and the magnetic susceptibility of carriers in inversion layers. *Journal of Physics C: Solid State Physics*, 17(33):6039, 1984.
- [9] Frank Wilczek and A. Zee. Appearance of Gauge Structure in Simple Dynamical Systems. *Physical Review Letters*, 52(24):2111–2114, June 1984.
- [10] Tudor D. Stănescu, Brandon Anderson, and Victor Galitski. Spin-orbit coupled Bose-Einstein condensates. *Physical Review A*, 78(2):023616, August 2008.
- [11] Tigran A. Sedrakyan, Alex Kamenev, and Leonid I. Glazman. Composite fermion state of spin-orbit-coupled bosons. *Physical Review A*, 86(6):063639, December 2012.
- [12] Hui Hu, Lei Jiang, Xia-Ji Liu, and Han Pu. Probing Anisotropic Superfluidity in Atomic Fermi Gases with Rashba Spin-Orbit Coupling. *Physical Review Letters*, 107(19):195304, November 2011.
- [13] Victor Galitski and Ian B. Spielman. Spin-orbit coupling in quantum gases. *Nature*, 494(7435):49–54, February 2013.
- [14] N. Goldman, G. Juzeliūnas, P. Öhberg, and I. B. Spielman. Light-induced gauge fields for ultracold atoms. *Reports on Progress in Physics*, 77(12):126401, November 2014.
- [15] D. L. Campbell, G. Juzeliūnas, and I. B. Spielman. Realistic Rashba and Dresselhaus spin-orbit coupling for neutral atoms. *Physical Review A*, 84(2):025602, August 2011.
- [16] Tudor D. Stănescu and Victor Galitski. Spin relaxation in a generic two-dimensional spin-orbit coupled system. *Physical Review B*, 75(12):125307, March 2007.
- [17] D. L. Campbell and I. B. Spielman. Rashba realization: Raman with RF. *New J. Phys.*, 18(3):033035, 2016.
- [18] Y.-J. Lin, A. R. Perry, R. L. Compton, I. B. Spielman, and J. V. Porto. Rapid production of $\text{\^87}\text{R} \text{b}$ Bose-Einstein condensates in a combined magnetic and optical potential. *Physical Review A*, 79(6):063631, June 2009.
- [19] Lianghui Huang, Zengming Meng, Pengjun Wang, Peng Peng, Shao-Liang Zhang, Liangchao Chen, Donghao Li, Qi Zhou, and Jing Zhang. Experimental realization of two-dimensional synthetic spin-orbit coupling in ultracold Fermi gases. *Nature Physics*, 12(6):540–544, June 2016.
- [20] Zengming Meng, Lianghui Huang, Peng Peng, Donghao Li, Liangchao Chen, Yong Xu, Chuanwei Zhang, Pengjun Wang, and Jing Zhang. Experimental Observation of a Topological Band Gap Opening in Ultracold Fermi

- Gases with Two-Dimensional Spin-Orbit Coupling. *Physical Review Letters*, 117(23):235304, December 2016.
- [21] Satoshi Tojo, Taro Hayashi, Tatsuyoshi Tanabe, Takuya Hirano, Yuki Kawaguchi, Hiroki Saito, and Masahito Ueda. Spin-dependent inelastic collisions in spin-2 Bose-Einstein condensates. *Physical Review A*, 80(4):042704, October 2009.
 - [22] Nigel R. Cooper and Jean Dalibard. Reaching Fractional Quantum Hall States with Optical Flux Lattices. *Physical Review Letters*, 110(18):185301, April 2013.
 - [23] N. Goldman and J. Dalibard. Periodically Driven Quantum Systems: Effective Hamiltonians and Engineered Gauge Fields. *Physical Review X*, 4(3):031027, 2014.
 - [24] A. Valdés-Curiel, D. Trypogeorgos, E. E. Marshall, and I. B. Spielman. Fourier transform spectroscopy of a spin-orbit coupled Bose gas. *New Journal of Physics*, 19(3):033025, 2017.
 - [25] N. Fläschner, B. S. Rem, M. Tarnowski, D. Vogel, D.-S. Lühmann, K. Sengstock, and C. Weitenberg. Experimental reconstruction of the Berry curvature in a Floquet Bloch band. *Science*, 352(6289):1091–1094, May 2016.
 - [26] Clément Godfrin, Rafik Ballou, Edgar Bonet, Mario Ruben, Svetlana Klyatskaya, Wolfgang Wernsdorfer, and Franck Balestro. Generalized Ramsey interferometry explored with a single nuclear spin qudit. *npj Quantum Information*, 4(1):53, October 2018.
 - [27] Takahiro Fukui, Yasuhiro Hatsugai, and Hiroshi Suzuki. Chern Numbers in Discretized Brillouin Zone: Efficient Method of Computing (Spin) Hall Conductances. *Journal of the Physical Society of Japan*, 74(6):1674–1677, June 2005.
 - [28] L. Duca, T. Li, M. Reitter, I. Bloch, M. Schleier-Smith, and U. Schneider. An Aharonov-Bohm interferometer for determining Bloch band topology. *Science*, 347(6219):288–292, January 2015.
 - [29] H. B. Nielsen and Masao Ninomiya. The Adler-Bell-Jackiw anomaly and Weyl fermions in a crystal. *Physics Letters B*, 130(6):389–396, November 1983.
 - [30] Mário G. Silveirinha. Chern invariants for continuous media. *Physical Review B*, 92(12):125153, September 2015.
 - [31] Pierre Delplace, J. B. Marston, and Antoine Venaille. Topological origin of equatorial waves. *Science*, 358(6366):1075–1077, November 2017.

- [32] Tigran A. Sedrakyan, Victor M. Galitski, and Alex Kamenev. Statistical Transmutation in Floquet Driven Optical Lattices. *Physical Review Letters*, 115(19):195301, November 2015.
- [33] Roger Brown. *Nonequilibrium many body dynamics with ultracold atoms in optical lattices and selected problems in atomic physics*. PhD thesis, University of Maryland College Park, Digital Repository at the University of Maryland, 6 2014.
- [34] Creston D. Herold. *Ultracold mixtures of Rubidium and Ytterbium for open system quantum engineering*. PhD thesis, University of Maryland College Park, Digital Repository at the University of Maryland, 6 2014.
- [35] Abigail R. Perry. *An apparatus for light-less artificial gauge fields and new imaging techniques*. PhD thesis, University of Maryland College Park, Digital Repository at the University of Maryland, 6 2015.
- [36] B. P. Anderson and M. A. Kasevich. Loading a vapor-cell magneto-optic trap using light-induced atom desorption. *Physical Review A*, 63(2):023404, January 2001.